

# Starbursting [O III] emitters and quiescent [C II] emitters in the reionization era

Shohei Arata<sup>1\*</sup>, Hidenobu Yajima<sup>2</sup>, Kentaro Nagamine<sup>1,3,4</sup>, Makito Abe<sup>2</sup>  
and Sadegh Khochfar<sup>5</sup>

<sup>1</sup> *Department of Earth and Space Science, Graduate School of Science, Osaka University, Toyonaka, Osaka 560-0043, Japan*

<sup>2</sup> *Center of Computational Sciences University of Tsukuba, Ibaraki 305-8577, Japan*

<sup>3</sup> *Department of Physics & Astronomy, University of Nevada, Las Vegas, 4505 S. Maryland Pkwy, Las Vegas, NV 89154-4002, USA*

<sup>4</sup> *Kavli IPMU (WPI), The University of Tokyo, 5-1-5 Kashiwanoha, Kashiwa, Chiba, 277-8583, Japan*

<sup>5</sup> *SUPA, Institute for Astronomy, University of Edinburgh, Royal Observatory, Edinburgh, EH9 3HJ, UK*

Accepted ?; Received ??; in original form ???

## ABSTRACT

Recent observations have successfully detected [O III] 88.3  $\mu\text{m}$  and [C II] 157.6  $\mu\text{m}$  lines from galaxies in the early Universe with the Atacama Large Millimeter Array (ALMA). Combining cosmological hydrodynamic simulations and radiative transfer calculations, we present relations between the metal line emission and galaxy evolution at  $z = 6\text{--}15$ . We find that galaxies during their starburst phases have high [O III] luminosity of  $\sim 10^{42}$  erg s<sup>-1</sup>. Once supernova feedback quenches star formation, [O III] luminosities rapidly decrease and continue to be zero for  $\sim 100$  Myr. The slope of the relation between  $\log(\text{SFR}/M_{\odot} \text{ yr}^{-1})$  and  $\log(L_{[\text{O III}]} / L_{\odot})$  at  $z = 6\text{--}9$  is 1.03, and 1.43 for  $\log(L_{[\text{C II}]} / L_{\odot})$ . As gas metallicity increases from sub-solar to solar metallicity by metal enrichment from star formation and feedback, the line luminosity ratio  $L_{[\text{O III}]} / L_{[\text{C II}]}$  decreases from  $\sim 10$  to  $\sim 1$  because the O/C abundance ratio decreases due to carbon-rich winds from AGB stars. Therefore, we suggest that the combination of [O III] and [C II] lines is a good probe to investigate the relative distribution of ionized and neutral gas in high- $z$  galaxies. In addition, we show that deep [C II] observations with a sensitivity of  $\sim 10^{-2}$  mJy arcsec<sup>-2</sup> can probe the extended neutral gas disks of high- $z$  galaxies.

**Key words:** hydrodynamics – galaxies: formation – galaxies: high-redshift – galaxies: evolution – galaxies: ISM – radiative transfer

## 1 INTRODUCTION

Understanding the physical properties of distant galaxies is one of the major goals of present astrophysical research. Observations of metal lines and dust continuum can be a useful tool to investigate the physical state of the ISM in distant galaxies. Recent ALMA observations have detected metal and dust in galaxies at  $z \gtrsim 6$  via the [C II] 158  $\mu\text{m}$  line (Willott et al. 2015; Carniani et al. 2017; Decarli et al. 2017; Knudsen et al. 2017; Smit et al. 2018; Marrone et al. 2018; Hashimoto et al. 2019), the [O III] 88  $\mu\text{m}$  line (Inoue et al. 2016; Carniani et al. 2017; Laporte et al. 2017; Hashimoto et al. 2018; Marrone et al. 2018; Hashimoto et al. 2019; Tamura et al. 2019), and dust continuum (Watson et al. 2015; Laporte et al. 2017; Bowler et al. 2018; Marrone et al. 2018; Hashimoto et al.

2019; Tamura et al. 2019). These observations can provide information about the physical state and star formation activities of galaxies. For example, the [C II] line is the main coolant for the warm ISM (Wolfire et al. 2003), and leads to the formation of the cold neutral medium (CNM) via thermal instabilities even in a low-metallicity environment (Arata et al. 2018). The confined CNM becomes molecular clouds, and forms stars. UV radiation from young stars subsequently produces O III regions. Therefore, combining [C II] and [O III] observations will help to understand the physical processes of star formation within a multi-phase ISM (e.g. Cormier et al. 2012).

Recent observations showed interesting features in high- $z$  galaxies. Inoue et al. (2016) reported [O III] detection for an Lyman- $\alpha$  emitter at  $z = 7.2$ , but [C II] was undetected. The upper limit of [C II] luminosity was much lower than the expected from the relation of local galaxies (De Looze et al. 2014). Laporte et al. (2019) also re-

\* E-mail: arata@astro-osaka.jp

ported the [C II] absence for two [O III] emitters at  $z \sim 9$  (see also, Laporte et al. 2017; Hashimoto et al. 2018). Meanwhile, Hashimoto et al. (2019) successfully detected both metal lines [C II] and [O III] (see also, Marrone et al. 2018; Smit et al. 2018; Tamura et al. 2019). These galaxies show a negative correlation between the luminosity ratio  $L_{[\text{O III}]} / L_{[\text{C II}]}$  and bolometric luminosity  $L_{\text{bol}}$ . The origin of these features has been a puzzle so far.

Some theoretical works studied metal emission lines from high- $z$  galaxies. Combining cosmological simulations and analytical model for the multi-phase ISM, Nagamine et al. (2006) predicted the ALMA observability of the [C II] line from star-forming galaxies at  $z = 3 - 6$ . Pallottini et al. (2017b) focused on properties of Lyman-Break Galaxies at  $z \sim 6$ . They used zoom-in simulations, and found that  $\text{H}_2$  galactic disk mainly contributed to the total [C II] luminosity (see also Pallottini et al. 2017a, 2019). Recently, Moriwaki et al. (2018) studied the observability of [O III] emitters at  $z \sim 8$  using a  $(50 h^{-1} \text{cMpc})^3$  simulation with a sub-grid model for the ionization structure. Very recently Katz et al. (2019) studied various metal emission lines at  $z \gtrsim 9$  using zoom-in radiative hydrodynamics simulations and CLOUDY, and found kpc-scale offsets between [O III] and [C II] emitting regions. However, their galaxy sample was limited due to the expensive calculation.

As stated above, observed high- $z$  galaxies were likely to have a wide variety of metal line properties. In this work, we calculate the metal line properties of 10 galaxies with zoom-in initial conditions and study the relation between metal lines and galaxy evolution. As suggested in the simulations of Yajima et al. (2017) (hereafter Y17), high- $z$  galaxies could repeat star-bursts, which results in galactic outflow due to SN feedback. This in turn quenches subsequent star formation, and results in intermittent star-formation histories (see also, Hopkins et al. 2014; Kimm & Cen 2014; Davis et al. 2014).

Combining hydrodynamic simulations of Y17 and radiative transfer calculations, Arata et al. (2019, hereafter A19) studied how the intermittent star formation affected UV and infrared SEDs. We found that the escape fraction of UV photons fluctuated due to changing dust distribution, which resulted in the fluctuations of IR luminosity. In this paper, we focus on how FIR metal emission lines ([O III]  $88 \mu\text{m}$  and [C I]  $158 \mu\text{m}$ ) are affected by the intermittent star formation.

Our paper is organized as follows. We describe our models for cosmological hydrodynamic simulations and radiative transfer calculations in Section 2. In Section 3, we present our results. In Sections 3.1 and 3.2, we focus on which gas phases contribute to total metal line luminosities ( $L_{\text{line}}$ ). In Section 3.3, we focus on the fluctuations of  $L_{\text{line}}$  due to intermittent star formation in first galaxies. We also show the relation between SFR and  $L_{\text{line}}$ , and discuss how  $L_{[\text{O III}]} / L_{[\text{C II}]}$  ratio decreases with metal enrichment. In Section 3.6, we discuss the  $L_{\text{line}} / L_{\text{IR}}$  ratio, which reflects the ratio of absorbed energy by gas or dust. In Section 3.7, we focus on the spatial distributions of metal emission lines. In addition, we discuss the dependence of our results on sub-grid models for star formation and SN feedback in Sec. 4.1. Finally, we summarise our main conclusions in Section 5.

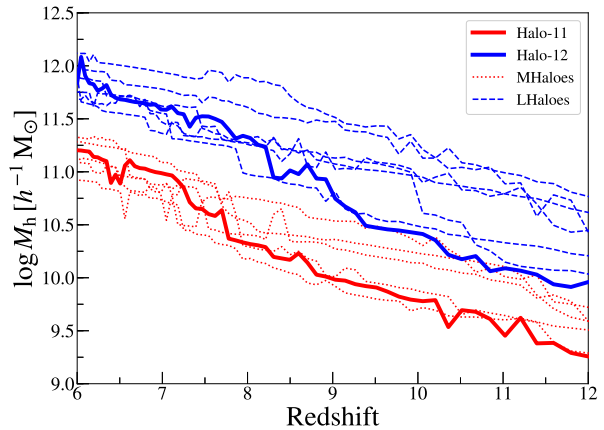


**Figure 1.** Mass growth of our haloes. Red lines represent haloes with total halo masses of  $M_h \sim 10^{11} M_\odot$  at  $z = 6$ , identified in  $(20 \text{cMpc})^3$  box. Blue lines are for haloes with  $M_h \sim 10^{12} M_\odot$  at  $z = 6$ , identified in  $(100 \text{cMpc})^3$  box. Thick lines represent our fiducial runs (Halo-11 and Halo-12). Table 1 shows detailed properties of these haloes.

## 2 METHOD

### 2.1 Cosmological hydrodynamic simulations

We use the GADGET-3 code (an updated version of GADGET-2 described in Springel 2005) with sub-grid models developed in the *Overwhelming Large Simulation* project (Schaye et al. 2010) and extended for the *First Billion Year* (FiBY) project to include sub-grid models for galaxy formation in the early Universe such as e.g. POP-III star formation and molecular networks (see e.g. Johnson et al. 2013; Paardekooper et al. 2015). The FiBY implementation reproduces general properties of the high- $z$  galaxy population well (see e.g. Cullen et al. 2017; Arata et al. 2019). We first focus on the two haloes presented in Y17, whose total masses are  $M_h \sim 10^{11} M_\odot$  and  $\sim 10^{12} M_\odot$  at  $z = 6$  (Halo-11 and Halo-12), and call them the *fiducial* runs. Halo-12 is identified as the most massive halo at  $z \approx 3.0$  with  $M_h \sim 1.3 \times 10^{13} h^{-1} M_\odot$  in a simulation box of comoving  $(100 \text{Mpc})^3$ . To increase our simulated galaxy samples, we perform additional cosmological hydrodynamic simulations. Here we briefly summarize our models.

We first conduct  $N$ -body simulations with box-sizes of  $(20 h^{-1} \text{Mpc})^3$  and  $(100 h^{-1} \text{Mpc})^3$ , and identify the four most massive haloes at  $z = 6$ . We call them MHalo-0, 1, 2, 3 and LHalo-0, 1, 2, 3, respectively. We also perform an additional  $N$ -body simulation with  $(100 h^{-1} \text{Mpc})^3$  box size until  $z = 3$  and identify the two most massive haloes with masses of  $1.8 \times 10^{13} h^{-1} M_\odot$  and  $1.3 \times 10^{13} h^{-1} M_\odot$ . We then recompute hydrodynamics in the zoom-in region until  $z = 6$  (LHalo-4, 5). We set the gravitational softening length to  $\epsilon_{\text{min}} = 200 \text{pc}$  in comoving units for every zoom runs.

Figure 1 shows the redshift evolution of halo masses. We observe differences in the growth rates between Halo-12 and the LHaloes, which we ascribe to the environments that they live in. This can be quantified by the mass overdensity  $\delta$  at  $z = 10$  within a sphere of radius  $1 \text{cMpc}$  centered on each halo:  $\delta = 2.02$  (for Halo-12), and  $\delta = 3.12, 2.50, 2.29, 2.20, 2.19$  and  $2.09$  for LHalo-0, 1, 2, 3,

Halo ID	$M_h$ [ $h^{-1} M_\odot$ ]	$m_{\text{DM}}$ [ $h^{-1} M_\odot$ ]	$m_{\text{gas}}$ [ $h^{-1} M_\odot$ ]	SNe feedback	$A$	$\delta$	$M_{1500}$ [mag]
Halo-11	$1.6 \times 10^{11}$	$6.6 \times 10^4$	$1.2 \times 10^4$	ON	$2.5 \times 10^{-3}$	1.52	-20.3
Halo-12	$6.9 \times 10^{11}$	$1.1 \times 10^6$	$1.8 \times 10^5$	ON	$2.5 \times 10^{-3}$	2.02	-22.1
MHalo-0	$2.1 \times 10^{11}$	$6.6 \times 10^4$	$1.2 \times 10^4$	ON	$2.5 \times 10^{-3}$	1.54	-20.4
MHalo-1	$1.9 \times 10^{11}$	$6.6 \times 10^4$	$1.2 \times 10^4$	ON	$2.5 \times 10^{-3}$	1.48	-20.4
MHalo-2	$1.3 \times 10^{11}$	$6.6 \times 10^4$	$1.2 \times 10^4$	ON	$2.5 \times 10^{-3}$	1.66	-20.2
MHalo-3	$1.2 \times 10^{11}$	$6.6 \times 10^4$	$1.2 \times 10^4$	ON	$2.5 \times 10^{-3}$	1.58	-20.3
LHalo-0	$1.3 \times 10^{12}$	$1.0 \times 10^6$	$1.8 \times 10^5$	ON	$2.5 \times 10^{-3}$	3.12	-23.2
LHalo-1	$9.3 \times 10^{11}$	$1.0 \times 10^6$	$1.8 \times 10^5$	ON	$2.5 \times 10^{-3}$	2.50	-22.5
LHalo-2	$7.9 \times 10^{11}$	$1.0 \times 10^6$	$1.8 \times 10^5$	ON	$2.5 \times 10^{-3}$	2.29	-22.0
LHalo-3	$5.7 \times 10^{11}$	$1.0 \times 10^6$	$1.8 \times 10^5$	ON	$2.5 \times 10^{-3}$	2.20	-21.0
LHalo-4	$8.0 \times 10^{11}$	$1.0 \times 10^6$	$1.8 \times 10^5$	ON	$2.5 \times 10^{-3}$	2.19	-20.3
LHalo-5	$4.9 \times 10^{11}$	$1.0 \times 10^6$	$1.8 \times 10^5$	ON	$2.5 \times 10^{-3}$	2.09	-21.2
Halo-11-lowSF	$1.5 \times 10^{11}$	$6.6 \times 10^4$	$1.2 \times 10^4$	ON	$2.5 \times 10^{-4}$	1.52	-19.5
Halo-11-noSN	$1.6 \times 10^{11}$	$6.6 \times 10^4$	$1.2 \times 10^4$	OFF	$2.5 \times 10^{-3}$	1.52	-21.0
Halo-12-lowSF	$8.0 \times 10^{11}$	$1.1 \times 10^6$	$1.8 \times 10^5$	ON	$2.5 \times 10^{-4}$	2.02	-21.7
Halo-12-noSN	$6.5 \times 10^{11}$	$1.1 \times 10^6$	$1.8 \times 10^5$	OFF	$2.5 \times 10^{-3}$	2.02	-22.4

**Table 1.** Parameters of our zoom-in cosmological hydrodynamic simulations: (1)  $M_h$  is the halo mass identified by the friends-of-friends method for dark matter particles at  $z = 6.0$ . (2)  $m_{\text{DM}}$  is the mass of a dark matter particle. (3)  $m_{\text{gas}}$  is the initial mass of a gas particle. (4)  $A$  is the amplitude factor in the star formation model based on the Kennicutt–Schmidt law (Schaye & Dalla Vecchia 2008). The Halo-11-lowSF and Halo-12-lowSF runs have a lower star formation amplitude factor. The Halo-11-noSN and Halo-12-noSN runs have no SN feedback. (5)  $\delta \equiv \rho/\rho_{\text{crit}}$  is the mass overdensity at  $z = 10$  within a sphere of radius 1 cMpc centered on the halo. (6)  $M_{1500}$  is the absolute magnitude at  $z = 6.0$  in rest-frame 1500 Å, obtained from radiative transfer.

4 and 5 respectively. The variance of the overdensity for LHalo-0, 1, 2 and 3 is  $\sigma_{1 \text{ Mpc}} = 1.57$ . From these values, it is evident that LHaloes live in more dense environments than Halo-12, which results in earlier growth of halo masses. At  $z \sim 6$ , Halo-12 catches up with LHaloes and achieves an intermediate halo mass among them.

Next we make zoom-in initial conditions with effective resolution of  $2048^3$  particles for  $(20 h^{-1} \text{Mpc})^3$  box and  $4096^3$  particles for  $(100 h^{-1} \text{Mpc})^3$  box using the MUSIC code (Hahn & Abel 2011), and carry out hydrodynamics simulations up to  $z = 6$ . The detailed information of the models is shown in Table 1.

The local star formation rate is calculated as (Schaye & Dalla Vecchia 2008)

$$\dot{m}_* = A(1 M_\odot \text{ pc}^{-2})^{-n} m_g \left( \frac{\gamma}{G} f_g P_{\text{tot}} \right)^{(n-1)/2}, \quad (1)$$

where  $\gamma$  is a specific heat index, and  $m_g$  is the mass of gas particle. The  $f_g$  is gas mass fraction in the self-gravitating galactic disk, and  $P_{\text{tot}}$  is total ISM pressure. This equation is based on the Kennicutt–Schmidt relation  $\dot{\Sigma}_* = A(\Sigma_g/1 M_\odot \text{ pc}^{-2})^n$  (Kennicutt 1998). We assume  $f_g = 1$  and  $n = 1.4$ . We also use  $A = 2.5 \times 10^{-3} M_\odot \text{ yr}^{-1} \text{ kpc}^{-2}$  as the fiducial value, which is 10 times higher than that of local star-forming galaxies, but recent observations have shown that higher values are preferred for merging or high- $z$  galaxies (e.g. Genzel et al. 2010; Tacconi et al. 2013). To check the impact of  $A$  on our main results, we also study a run with  $A = 2.5 \times 10^{-4} M_\odot \text{ yr}^{-1} \text{ kpc}^{-2}$  (indicated as ‘low-SF’ in Table 1). Our star formation threshold density is  $n_{\text{H}} = 10 \text{ cm}^{-3}$  (Johnson et al. 2013).

Our simulations track the abundances of 9 elements (H, He, C, N, O, Ne, Mg, Si and Fe) for each particle separately (Wiersma et al. 2009b). The sources of chemical enrichment are Type-Ia/II SNe, and AGB stars (Portinari et al. 1998;

Marigo 2001). For  $z \gtrsim 6$  galaxies, it is dominated by Type-II SNe, because it takes  $\sim 10^9$  yrs to become AGB stars for low- and intermediate-mass stars. However, as we will show later, the AGB star contribution is important for some of the abundance ratio, such as O/C. In this paper, we consider all of the above chemical sources in our calculations of metal line luminosities (Sec. 2.3, 2.4).

SN feedback injects thermal energy into neighbouring gas particles stochastically (Dalla Vecchia & Schaye 2012), and the gas temperature increase to  $10^{7.5} \text{ K}$ . The thermal energy is efficiently converted into kinetic energy against radiative cooling, if the gas density is lower than the critical value of  $n_{\text{H}} \sim 100 \text{ cm}^{-3} (T/10^{7.5} \text{ K})^{3/2} (m_g/10^4 M_\odot)^{-1/2}$ . The numerical resolution of our simulations are adequate to successfully launch galactic winds and suppress star formation (see Y17). We further perform simulations without SN feedback to investigate the impact on metal line properties (indicated as ‘no-SN’ in Table 1).

## 2.2 Radiative transfer

In next sub-sections, we model metal emissions based on the ionization structure of hydrogen gas. To obtain it, we use the radiative transfer code, All-wavelength Radiative Transfer with Adaptive Refinement Tree (ART<sup>2</sup>) code (Li et al. 2008; Yajima et al. 2012b). The details of this code were described in A19.

The ART<sup>2</sup> is based on the Monte Carlo technique. It tracks propagation of photon packets emitted from stellar particles, and computes the emergent SED. The intrinsic SED for each stellar particle is taken from STARBURST99 (Leitherer et al. 1999) assuming the Chabrier initial mass function with a mass range of  $0.1 - 100 M_\odot$  (Chabrier 2003). ART<sup>2</sup> calculates the transfer of ionizing photons, UV continuum and dust absorption/re-emission using adaptive mesh

refinement (AMR) cells. The spatial resolution of the minimum size cells is set to physical  $2.7 h^{-1} \text{pc}$  for Halo-11 at  $z = 6$ . We assume that the dust-to-gas mass ratio  $\mathcal{D}$  is proportional to gas metallicity as seen in local galaxies,  $\mathcal{D} = 8 \times 10^{-3} (Z/Z_{\odot})$  (Draine et al. 2007). In addition, we multiply the neutral fraction of hydrogen in a local cell to  $\mathcal{D}$  considering that the dust abundance is much lower in ionized regions (Burke & Silk 1974; Reynolds et al. 1997).

### 2.3 [O III] emission model

UV photons from massive stars create [O III] regions. Therefore, the [O III] luminosity is likely to be related closely with star formation activity. Recent observations successfully detected [O III] lines and confirmed the redshifts of distant galaxies even at  $z \gtrsim 7$  (e.g., Hashimoto et al. 2018). Since the ionization potential of  $\text{O}^+ \rightarrow \text{O}^{2+}$  is 35.121 eV,  $\text{O}^{2+}$  ions exist only in H II regions. Based on the photo-ionization radiative transfer calculations (Sec. 2.2), we classify all cells into ‘H I cell’ and ‘H II cell’ according to their hydrogen neutral fractions, separated at the value of 0.5. Next we calculate doubly ionized fraction of oxygen in each H II cell assuming ionization equilibrium between  $\text{O}^+$  and  $\text{O}^{2+}$ <sup>1</sup>:

$$\int_{\nu_{\min}}^{\infty} n_{\text{O}^+} \frac{\sigma_{\nu} F_{\nu}}{h\nu} d\nu = \alpha(T) n_e n_{\text{O}^{2+}}. \quad (2)$$

The left hand side represents the photo-ionization rate per volume, where  $\nu_{\min} = 8.492 \times 10^{15} \text{ Hz}$  is the minimum frequency for ionization. For the photo-ionization cross section  $\sigma_{\nu}$  we use the fitting function derived in Verner et al. (1996) (same as in CLOUDY, Ferland et al. 1998; Richings et al. 2014). We evaluate the flux  $F_{\nu}$  using the optically-thin approximation and sum up contributions from nearby stellar particles:

$$F_{\nu} = \sum_{R_j < R_S} F_{\nu,j} = \sum_{R_j < R_S} \frac{L_{\nu,j}}{4\pi R_j^2}, \quad (3)$$

where  $L_{\nu,j}$  is the specific luminosity of the  $j$ -th stellar particle, and  $R_j$  is the distance from the cell. In the above estimation, we calculate the radius of the Strömngren sphere as  $R_S = (3Q_0/4\pi n_{\text{H}}^2 \alpha_B)^{1/3}$ , where  $Q_0$  ( $s^{-1}$ ) is the ionizing photon emission rate of nearby stars. If the radius reaches a target cell, the flux from stars in the nearby cell is considered using the above equation. We need this condition to exclude the contributions from stellar particles in the other H II regions, because their UV radiation should be interrupted by intervening neutral gas. The right hand side of Eq. (2) represents recombination rate per volume, where  $\alpha(T)$  is the coefficient as a function of temperature (Nahar & Pradhan 1997; Nahar 1999).

The  $\text{O}^{2+}$  ground state has three fine-structures:  $^3\text{P}_0$ ,  $^3\text{P}_1$ , and  $^3\text{P}_2$ . The  $88 \mu\text{m}$  FIR line is emitted via the  $^3\text{P}_1 \rightarrow ^3\text{P}_0$  transition. We calculate the rate equations among three levels (Nussbaumer & Storey 1981), and obtain the level populations. Local [O III] luminosity from a H II cell is estimated by

$$L = (C_{\text{lu}} n_{\text{l}} - C_{\text{ul}} n_{\text{u}}) \beta h\nu_{\text{ul}} V_{\text{cell}}, \quad (4)$$

<sup>1</sup> Here we neglect the O I abundance, because the ionization potential is similar to that of H I ( $\Phi_0 = 13.6181 \text{ eV}$ ), and most O I atoms are ionized in H II region.

where  $C_{\text{lu}}$  ( $C_{\text{ul}}$ ) is the Einstein coefficient of collisional excitation (de-excitation) which depends on electron density. The  $V_{\text{cell}}$  is the cell volume, and  $\beta$  is the escape probability, for which we assume optically thin case of  $\beta = 1$ . In addition, if gas temperature is higher than  $1.2 \times 10^5 \text{ K}$ , we set the luminosity to zero because the ionization degree of oxygen is triple or higher (Nahar 1999). We confirmed that our model calculation result of the [O III] luminosity is almost the same as those from CLOUDY (see Appendix A).

### 2.4 [C II] emission model

The [C II]  $158 \mu\text{m}$  FIR line can be radiated from gas in various phases, i.e., warm neutral and ionized medium, CNM and molecular clouds (e.g. Wolfire et al. 2003), thus the modeling is relatively difficult. Previous theoretical work studied the contributions from each component with cosmological hydrodynamics simulations (Olsen et al. 2017; Pallottini et al. 2017a; Katz et al. 2019). Olsen et al. (2017) showed that diffuse ionized gas and molecular clouds were the main contributors to the [C II] luminosity. Observational constrains on the contributions suffer from the difficulty of determining the optical depth to the line (e.g. Neri et al. 2014).

The [C II] emission model is similar to that of [O III] emission described in previous sub-section. However, in the case of [C II], we consider both H I and H II cells as the emission sites. For the H II cells, we calculate the ionization equilibrium between  $\text{C}^+$  and  $\text{C}^{2+}$  under the stellar radiation field (Eq. 2). Meanwhile, we assume that all carbons are in  $\text{C}^+$  ions for H I cells. In our Galaxy, carbons are almost completely in  $\text{C}^+$  ions under the FUV ( $G_0 = 0.6 \text{ Habing}$ ) and cosmic ray background which are radiated by nearby star-forming regions and external galaxies (e.g. Webber 1998; Seon et al. 2011). Thus our assumption is valid for main-sequence galaxies, or at least provide an upper limit of the [C II] luminosity.

The [C II]  $158 \mu\text{m}$  line is radiated via the transition  $^2\text{P}_{3/2} \rightarrow ^2\text{P}_{1/2}$ . The luminosity is calculated as in Eq. 4. If the temperature of a cell is higher than  $4.0 \times 10^4 \text{ K}$ , the luminosity is set to zero because carbons are collisionally ionized to double or higher (Nahar & Pradhan 1997). Here we adopt the optically-thin approximation for the [C II]  $158 \mu\text{m}$  line, i.e.,  $\beta = 1$ . Note that, however, Neri et al. (2014) suggested that the optical depth for an observed  $z \sim 5.2$  galaxy could be  $\tau_{[\text{C II}]} \gtrsim 1$ . If this is common in high- $z$  galaxies, our model may somewhat overestimate the [C II] luminosity. In addition, we also note that the cosmic microwave background (CMB) can affect [C II] emission (e.g. Goldsmith et al. 2012; da Cunha et al. 2013). As the redshift increases, the CMB temperature ( $T_{\text{CMB}} = 2.73(1+z) \text{ K}$ ) approaches the equivalent temperature of [C II] emission ( $T_{\text{eq}} = 91.2 \text{ K}$ ). Thus stimulated emission/absorption can be significant for  $z \gtrsim 6$  galaxies (Vallini et al. 2015; Lagache et al. 2018). In Appendix B, we estimate the CMB effect and find the the CMB reduces the luminosity only by a few percent.



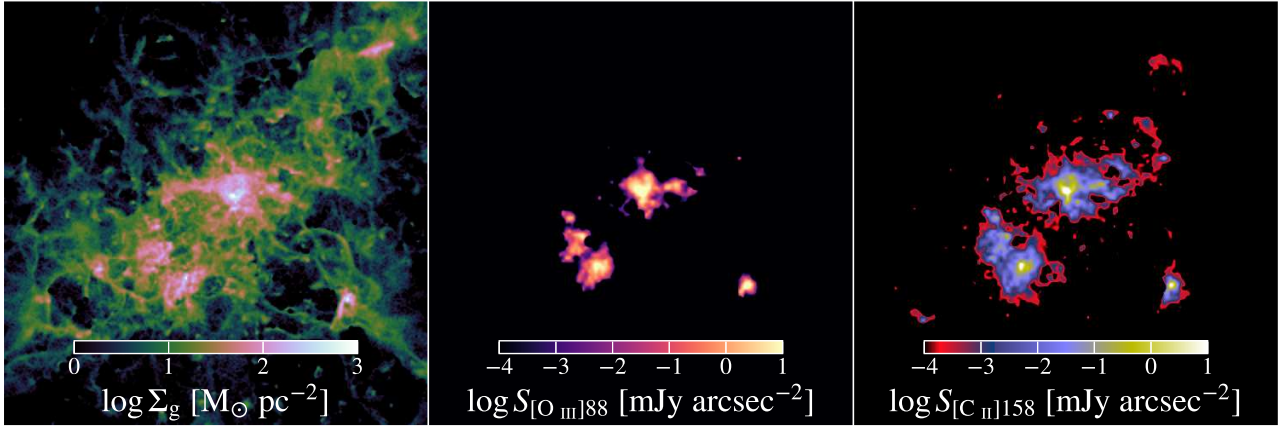


**Figure 2.** Maps of the main halo in Halo-11 run at  $z = 6.0$ . *Left panel:* Gas surface density. The spacial scale is 51 physical kpc. *Middle & right panels:* Intensity maps of [O III] 88  $\mu\text{m}$  and [C II] 158  $\mu\text{m}$  lines, respectively. The pixel size is  $\sim 0.07$  arcsec, which corresponds to  $\sim 0.4$  physical kpc.

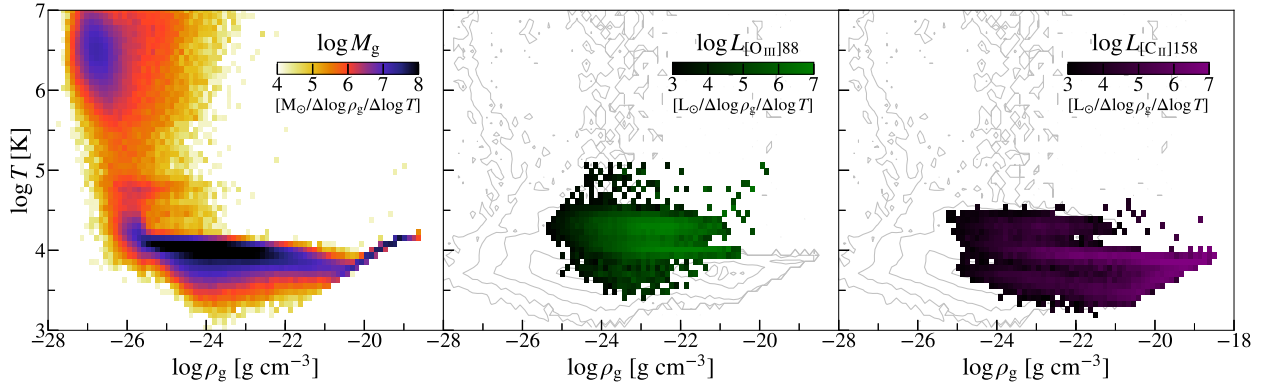


**Figure 3.** *Left panel:* Gas phase diagram for Halo-11 at  $z = 6.0$ . *Middle & right panels:* Gas phases emitting [O III] 88  $\mu\text{m}$  and [C II] 158  $\mu\text{m}$  lines, respectively. The gray contour shows gas phases after the ionization radiative transfer calculation, where five levels of contour correspond to the following gas mass in each pixel:  $\log M_g [\text{M}_\odot / \Delta \log \rho_g / \Delta \log T] = 4, 5, 6, 7 \text{ \& } 8$ .

### 3 RESULT

#### 3.1 Projected Images

The left panel of Figure 2 presents a 2-D map of gas column density in Halo-11 at  $z = 6.0$ . The total stellar mass, gas mass, and dust mass are  $M_\star = 2.2 \times 10^9 h^{-1} \text{M}_\odot$ ,  $M_{\text{gas}} = 1.1 \times 10^{10} h^{-1} \text{M}_\odot$  and  $M_{\text{dust}} = 9.6 \times 10^6 h^{-1} \text{M}_\odot$ . The gas structure shows filaments and clumps, and extends over  $\sim 20$  kpc. The middle and right panels show the surface brightness of [O III] 88  $\mu\text{m}$  and [C II] 158  $\mu\text{m}$ , which represent ionized and neutral regions (see Fig. 3.2), and the brightest pixels have 157.6 and 485.7  $\text{mJy arcsec}^{-2}$ , respectively. We find that the [O III] map is sharply cut off at high-density regions of  $\Sigma_{\text{gas}} \gtrsim 10^2 \text{M}_\odot \text{pc}^{-2}$  (white in the left panel). In addition, future deep [C II] observations with a sensitivity of  $\lesssim 10^{-2} \text{mJy arcsec}^{-2}$  will be able to probe the structure of extended cold gas disks over  $\sim 10$  kpc (pink in the left panel).

#### 3.2 Physical properties of gas with metal-line emission

The left panel of Figure 3 shows the phase diagram of gas in Halo-11 at  $z = 6.0$ . The hot ionized medium ( $T \sim 10^6 - 10^7 \text{K}$ ) cools down to  $\sim 10^4 \text{K}$  via metal cooling (Wiersma et al. 2009a) and hydrogen Ly $\alpha$  cooling. Star formation occurs in dense gas clouds ( $n_{\text{H}} \gtrsim 10 \text{cm}^{-3}$ ). The star-forming clouds contracts based on the effective equation of state (Schaye & Dalla Vecchia 2008). Due to SN feedback, the gas near young stars is returned to the hot phase. In this work, we consider the photo-ionization of gas due to young stars by post-processing, and heating up the gas to  $\sim 2 \times 10^4 \text{K}$  if the ionization degree of hydrogen exceeds 0.99. The corrected gas temperature is shown by the gray contours in the middle and right panels. In addition, we do not consider the UV background in our RT calculations, which would be important for the ionization state of the IGM (Haardt & Madau 2012). However, we are interested in gas at densities higher than that for self-shielding ( $n \sim 10^{-2} \text{cm}^{-3}$ , Nagamine et al. 2010; Altay et al. 2011; Yajima et al. 2012a; Bird et al. 2013; Rahmati et al. 2013).

Thus our conclusions do not change by neglecting the effect of the UVB.

The middle panel of Fig. 3 shows the physical state of gas emitting the [O III] line. The total luminosity is  $2.26 \times 10^{42} \text{ erg s}^{-1}$ , and the half of it is contributed by completely ionized gas ( $x_e > 0.99$ ). The right panel shows [C II] emitting phases. The total luminosity is  $2.0 \times 10^{42} \text{ erg s}^{-1}$ , and its 99% is contributed by the neutral gas ( $x_e < 0.5$ ). In particular, the gas clouds with  $n_{\text{H}} \gtrsim 10^3 \text{ cm}^{-3}$  are the main contributor (88%) to the total luminosity. Since the density is higher than the critical density for thermalization of  $158 \mu\text{m}$  fine-structure transition ( $\sim 10^3 \text{ cm}^{-3}$ , see Fig. B1), the cooling rate per hydrogen atom is saturated. Observationally, Croxall et al. (2017) studied the contribution from neutral gas using local star-forming galaxies, and showed that it decreased from  $\sim 0.9$  to  $\sim 0.6$  as gas metallicity increased from  $12 + \log(\text{O}/\text{H}) \sim 8.0$  to 8.6. The metallicity of Halo-11 at  $z = 6.0$  is  $12 + \log(\text{O}/\text{H}) \approx 8.1$ . Thus our simulations are consistent with the observational result. This trend is also consistent with other simulation works (Olsen et al. 2017; Pallottini et al. 2017a; Katz et al. 2019). In addition to the previous works, we show that the metal-line luminosities rapidly change due to SN feedback as shown in the next sub-section.

### 3.3 Redshift Evolution of Metal Emission Lines

As shown in A19, UV and IR continuum flux from high- $z$  galaxies rapidly change due to the intermittent star formation history and SN feedback. Here we study the time evolution of metal lines. The top panel of Figure 4 shows the redshift evolution of the SFR of Halo-11 at  $z = 6 - 15$ . SN feedback evacuates most of the gas in galaxies and quenches star formation. The galaxy repeats the cycle of starburst and quenching at  $z \gtrsim 10$ . The time-scale of fluctuation is  $\sim 100 \left(\frac{1+z}{10}\right) \text{ Myr}$  which corresponds to the free-fall time of the halo. As the halo mass increases, the deep gravitational potential holds the gas against SN feedback, resulting in more continuous star formation (see Arata et al. 2019, for details).

The middle panel of Fig. 4 shows the escape fraction of ionizing (Lyman-continuum) photons. During the star-burst phases, ionizing photons are efficiently absorbed by dusty clouds surrounding star-forming regions, while  $f_{\text{esc}}$  increases during outflow phases because SN feedback makes holes allowing photons to escape. This results in the fluctuation of  $f_{\text{esc}}$  between  $\sim 0.01 - 0.6$  at  $z > 10$ .

At  $z = 11$ , the gas structure becomes filamentary, and star formation occurs in the knots as shown in Fig. 5. The ionizing photons efficiently escape into the perpendicular direction to the filament ( $f_{\text{esc}} \sim 40\%$ ). As described in the previous sections, the [O III] and [C II] lines are emitted from ionized regions (knots) and neutral gas (filament), respectively. Thus we suggest that the combination of [O III] and [C II] observations will reveal the neutral and ionized gas distribution, and indicate the escaping direction of ionizing photons. In addition, other simulations, which include radiative feedback from massive stars, have suggested rapid expansion of H II bubbles (e.g. Hopkins et al. 2014). This implies extended low-density [O III] regions. Meanwhile, our simulations predict very compact and high-density regions with  $n \gtrsim 10 \text{ cm}^{-3}$ , extending over  $\sim 5$  physical kpc with a

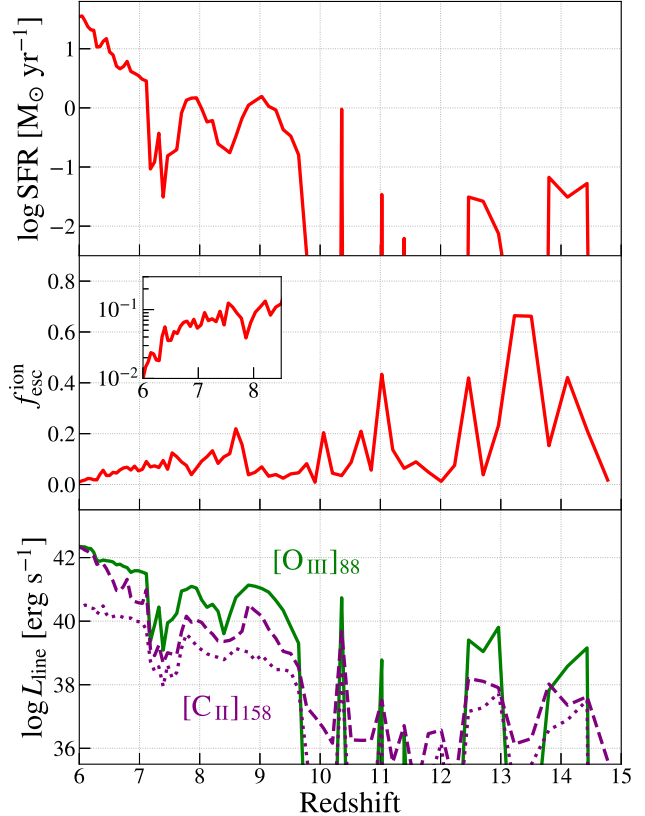


**Figure 4.** Redshift evolution of SFR (*top*), escape fraction of ionizing photons (*middle*), metal-line luminosities (*bottom*) for Halo-11. In the middle panel, the inset shows the escape fraction at  $z = 6 - 8$  in logarithmic-scale. In the bottom panel, green solid line represents [O III]  $88 \mu\text{m}$  luminosity. Purple dashed line is for [C II]  $158 \mu\text{m}$  luminosity. Dotted line shows the contribution to [C II] luminosity from H II regions.

surface brightness of  $\gtrsim 1 \text{ mJy arcsec}^{-2}$  at  $z = 6$ . Thus we suggest that the comparison of size and surface brightness of [O III] regions with observations can help constrain physical models of radiative feedback in high- $z$  galaxies.

At  $z < 10$ ,  $\langle f_{\text{esc}} \rangle$  decreases to  $\sim 1\%$  as the halo mass increases, which is consistent with the literature (e.g. Yajima et al. 2011, 2014; Paardekooper et al. 2015). In addition, as shown in A19, dusty gas is held in the massive halo against SN feedback, and the dust efficiently absorbs ionizing photons.

The bottom panel of Fig. 4 shows the [O III] and [C II] luminosities. The [O III] line is emitted only in the star-bursting phase because  $\text{O}^{2+}$  ions exist in H II regions formed by massive stars. We find that  $L_{[\text{O III}]}$  fluctuates with intermittent star formation in the range of  $10^{40} - 10^{42} \text{ erg s}^{-1}$  at  $z < 10$  for Halo-11. Meanwhile, the main source of [C II] emission is neutral gas, thus it is continuously emitted even in the outflowing phase. The contribution of [C II] emission from H II regions to the total luminosity (dotted line) increases during the star-bursting phase, but it does not exceed 50% over all redshifts. It gradually decreases with time due to dust absorption and results in  $\lesssim 2\%$  at  $z = 6$ .

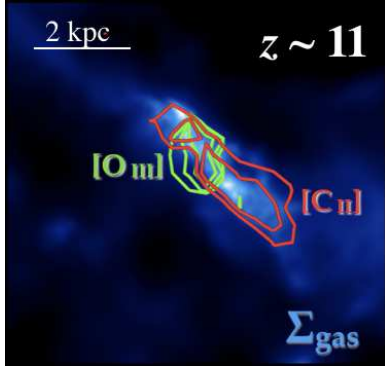


**Figure 5.** Contours of [O III] and [C II] intensity maps of Halo-11 at  $z = 11$ . The background picture shows the gas column density. The [C II] contour traces the filamentary neutral gas, and [O III] traces more knotty ionized regions corresponding to H II regions.

### 3.4 Metal-line luminosity vs. SFR

Figures 6 and 7 present [O III] and [C II] luminosities vs. SFR for Halo-11 and Halo-12 at  $z = 6, 7, 8$  and 9. Our simulations reproduce the observed luminosities well at  $z \gtrsim 6$ . In particular, Halo-12 shows  $L_{[\text{O III}]} = 2.3 \times 10^9 L_\odot$ ,  $L_{[\text{C II}]} = 1.7 \times 10^9 L_\odot$ , and  $L_{\text{IR}} = 6.9 \times 10^{11} L_\odot$  at  $z = 7$ , which are remarkably consistent with B14-65666 at  $z = 7.15$  ( $L_{[\text{O III}]} = 2.9 \times 10^9 L_\odot$ ,  $L_{[\text{C II}]} = 1.3 \times 10^9 L_\odot$ , and  $L_{\text{IR}} = 6.2 \times 10^{11} L_\odot$ ) as reported by Hashimoto et al. (2019). Also we compare our results with the relation of local galaxies derived in De Looze et al. (2014). They investigated low-metal galaxies in the range of  $-3 \lesssim \log \text{SFR} [M_\odot \text{ yr}^{-1}] \lesssim 2$  from the *Herschel* Dwarf Galaxy Survey. Our simulations are similar to metal-poor dwarf galaxies rather than local starburst galaxies. This result is consistent with Moriwaki et al. (2018), but is opposite to those of (Olsen et al. 2017; Katz et al. 2019). The chemical abundance pattern of galaxies at  $z > 6$  is dominated by Type-II SNe, and quite different from the solar neighbourhood. In the calculation of [O III] luminosity, we use the oxygen abundance of each gas particle, which is the same treatment as in Moriwaki et al. (2018) but not as in Olsen et al. (2017) and Katz et al. (2019). The oxygen abundance (mass-weighted mean) of Halo-12 evolves from  $12 + \log_{10}(\text{O}/\text{H}) = 6.6$  at  $z = 9$  to 8.9 at  $z = 6$ , and the range is close to that of local relation of  $12 + \log_{10}(\text{O}/\text{H}) = 7.14 - 8.43$  (De Looze et al. 2014). Thus we suggest that the physical state of the ISM in the first galaxies might be similar to that of local dwarf galaxies.

From the least-square fitting to all samples (Halo-11, Halo-12, MHaloes, LHaloes) at  $z = 6 - 9$ , we derive the following relations:

$$\log(L_{[\text{O III}]} [L_\odot]) = 7.23 + 1.04 \log(\text{SFR} [M_\odot \text{ yr}^{-1}]), \quad (5)$$

$$\log(L_{[\text{C II}]} [L_\odot]) = 6.38 + 1.47 \log(\text{SFR} [M_\odot \text{ yr}^{-1}]). \quad (6)$$

We find that [O III] luminosity is linearly proportional to the SFR, because most of the ionizing photons are absorbed by gas ( $f_{\text{esc}}^{\text{ion}} \lesssim 0.1$ ) for all of the galaxies. These fits nicely match the observed results at  $z \sim 6 - 9$  (Harikane et al. 2019). The  $L_{[\text{O III}]}-\text{SFR}$  relation at high- $z$  is very close to the relation for local metal-poor dwarf galaxies, while the slope of  $L_{[\text{C II}]}-\text{SFR}$  relation is steeper than the local ones

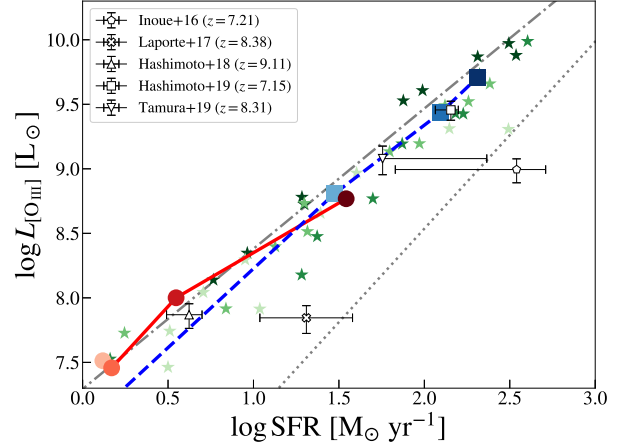


**Figure 6.** Relation between SFR and [O III] luminosity. Red circles (solid line) represent the evolution for Halo-11 at  $z = 9, 8, 7, 6$  (from lighter to darker). Blue squares (dashed line) are for Halo-12. Green stars are for other 10 samples at  $z = 6 - 9$ . Open black symbols represent the observed high- $z$  galaxies. Gray dotted line and dot-dashed line are for the local starburst galaxies and metal-poor dwarf galaxies, respectively (De Looze et al. 2014).

(1.0 for starburst galaxies and 1.25 for metal-poor galaxies, De Looze et al. 2014). In addition, these results are also supported by a more statistical study using semi-analytical models (Lagache et al. 2018).

Note that if efficient absorption is a common feature for high- $z$  galaxies, any deviation from Chabrier IMF would be reflected in the first term of Eq. (5). In other words, a top-heavy IMF predicts higher [O III] luminosity at a specific SFR, because more gas clouds would be ionized. Therefore a good observational estimate of this relationship can teach us a lot about the physics of star formation in high- $z$  galaxies. The same is also true for Eq. (6), which includes the contribution from accreting cold gas ( $\sim 10^4 \text{ K}$ ) (e.g. Dekel & Birnboim 2006). A higher normalization of Eq. (6) points toward higher accretion rates from cold accretion, and we can also expect this relation to change with redshift slightly.

### 3.5 [O III] and [C II] luminosity ratio

In this subsection, we focus on the [O III] and [C II] luminosity ratio. Hashimoto et al. (2019) showed the negative correlation between  $L_{[\text{O III}]} / L_{[\text{C II}]}$  and bolometric luminosity  $L_{\text{bol}}$  for galaxies at  $z > 6$ , in range of  $10^{10} L_\odot < L_{\text{bol}} < 10^{14} L_\odot$  (see also Marrone et al. 2018). The luminosity ratio can reflect the multi-phase ISM structure (e.g. Cormier et al. 2012). Cormier et al. (2015) found the same trend in local star-forming galaxies, and suggested that it depended on gas metallicity. Here we suggest that the origin of the negative correlation of high- $z$  galaxies is the carbon enrichment by AGB stars.

Figure 8 presents the  $(L_{[\text{O III}]} / L_{[\text{C II}]}) - L_{\text{bol}}$  relation at  $z = 6 - 9$ , where  $L_{\text{bol}}$  is measured from  $L_{\text{UV}} + L_{\text{IR}}$ . We find that  $L_{[\text{O III}]} / L_{[\text{C II}]}$  ratio decreases from  $\sim 10$  to  $\sim 1$  in the range of  $10 \lesssim \log(L_{\text{bol}} [L_\odot]) \lesssim 12$  with increasing metallicity from

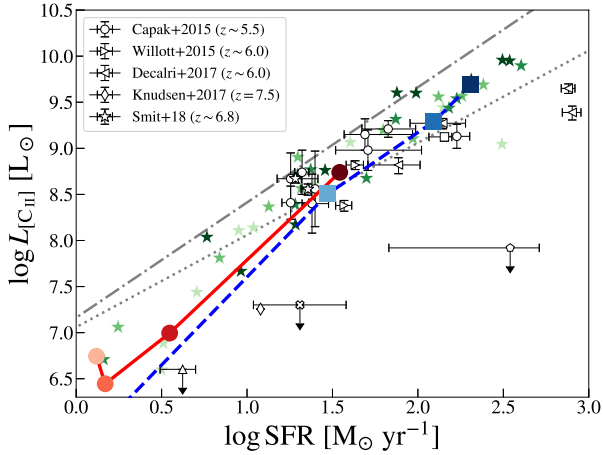


**Figure 7.** Relation between SFR and [C II] luminosity. The meaning of symbols is the same as in Fig. 6.

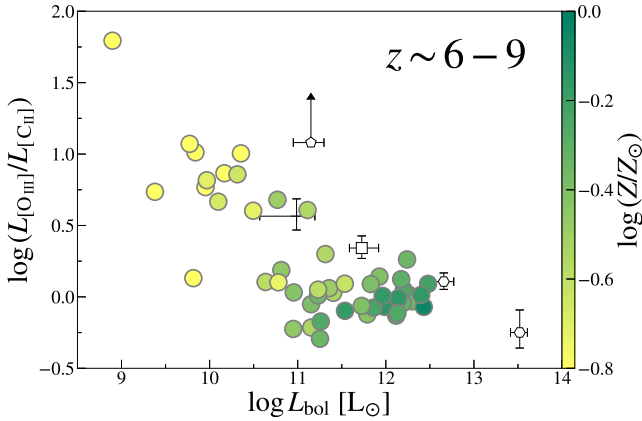


**Figure 8.** Relation between  $L_{[\text{O III}]} / L_{[\text{C II}]}$  ratio and bolometric luminosity ( $L_{\text{bol}} = L_{\text{UV}} + L_{\text{IR}}$ ). Filled circles represent our simulation samples at  $z \approx 6 - 9$ . The color is scaled by gas metallicity, which is an indicator of galactic evolution. The origin of the anti-correlation is carbon enrichment by AGB stars (see the main text). The open symbols represent observed galaxies at  $z \sim 6 - 9$  (Inoue et al. 2016; Carniani et al. 2017; Marrone et al. 2018; Hashimoto et al. 2019).

$\sim 0.1 Z_{\odot}$  to  $\sim 1 Z_{\odot}$ . The  $\log(L_{[\text{C II}]} / \text{SFR} [L_{\odot} / M_{\odot} \text{ yr}^{-1}])$  increases from 6.1 to 7.8, while  $\log(L_{[\text{O III}]} / \text{SFR})$  is constant ( $\sim 7.25 \pm 0.25$ ). The lower-mass galaxies has higher O/C ratio because Type-II SNe efficiently enrich the ISM with oxygen than carbon. As the galaxy evolves, low- and intermediate-mass stars begin to eject carbon-rich winds by dredge-up events of AGB phases (see also, Berg et al. 2019). The  $\log(\text{O}/\text{C})$  decreases from  $\sim 0.9$  to  $\sim 0.5$  when metallicities increase from  $\sim 0.1 Z_{\odot}$  to  $\sim 1 Z_{\odot}$ , therefore the  $L_{[\text{O III}]} / L_{[\text{C II}]}$  ratio decreases (Figure 10). To confirm the validity of this scenario, we use the Chemical Evolution Library (CELib, Saitoh 2017), and compute  $\log(\text{O}/\text{C})$  in a star-forming cloud with  $Z = 0.1 Z_{\odot}$  and the Chabrier IMF. The  $\log(\text{O}/\text{C})$  decreases from  $\sim 1.0$  to  $\sim 0.5$  when the age exceeds  $\sim 0.5$  Gyr which corresponds to half of the cosmic time at  $z \sim 6$ . This result supports our simulation results.

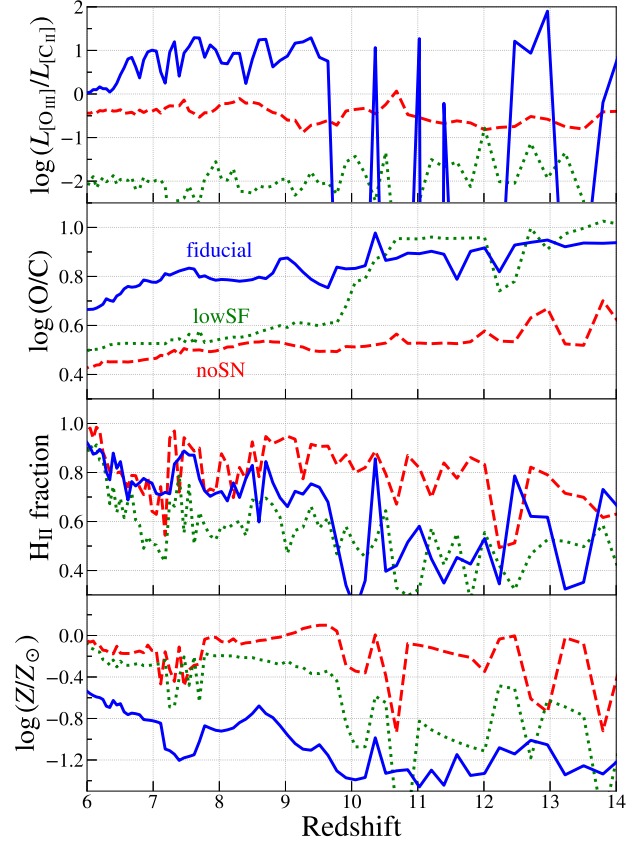


**Figure 9.** Redshift evolution of  $L_{[\text{O III}]} / L_{[\text{C II}]}$  ratio (top), O/C abundance ratio (second), volume fraction of H II regions (third), and gas metallicity within the halo (bottom). The solid blue line represents evolution of Halo-11, and red dashed and green dotted lines are for Halo-11-noSN and Halo-11-lowSF cases, respectively.

Our simulations are in good agreement with high- $z$  observations. The dependence on metallicity is also consistent with the local trend (Cormier et al. 2015), however our  $L_{[\text{O III}]} / L_{[\text{C II}]}$  ratio at a specific  $L_{\text{bol}}$  is  $\sim 10$  times higher than the local relation. Our samples have high ionization parameter ( $-2.2 \lesssim \log U \lesssim -1.5$ , where  $U$  is mean ionization parameter weighted by [O III] luminosity) and high volume fraction of H II regions ( $0.64 \lesssim f_{\text{H II}} \lesssim 1.0$ ). Using CLOUDY models, Harikane et al. (2019) suggested that galaxies with high- $U$  and low covering fraction of PDR can explain higher  $L_{[\text{O III}]} / L_{[\text{C II}]}$  ratio than local galaxies. Our results are consistent with Harikane’s picture of the first galaxies.

Figure 9 describes more details of redshift evolution of  $L_{[\text{O III}]} / L_{[\text{C II}]}$  ratio. The top panel shows that  $L_{[\text{O III}]} / L_{[\text{C II}]}$  ratio largely fluctuates with intermittent star formation in case of Halo-11 (blue line). But it gradually decreases with decreasing redshift due to carbon enrichment by AGB winds (second panel). The changes of volume fraction of H II regions (third panel) and gas density generate weak fluctuations of  $L_{[\text{O III}]} / L_{[\text{C II}]}$  ratio at  $z < 10$ . Due to continuous star formation at  $z < 10$ , gas in Halo-11 is highly ionized ( $f_{\text{H II}} \gtrsim 0.7$ ). The bottom panel shows that the gas metallicity in the halo gradually increases from  $z \sim 10$  towards lower redshift, because metal-enriched gas ejected by SN feedback



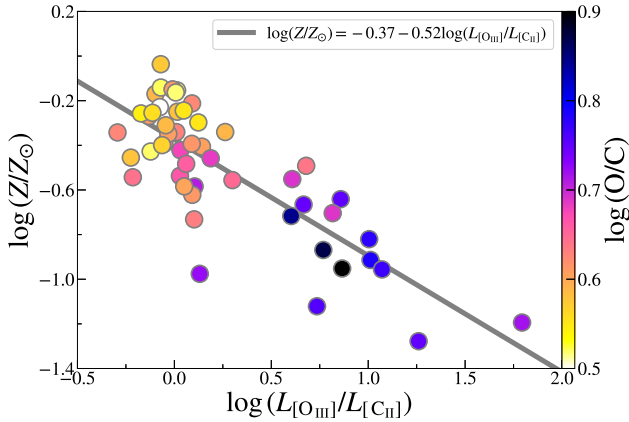


**Figure 10.** Relation between  $L_{[\text{O III}]} / L_{[\text{C II}]}$  ratio and total metallicity in our simulation samples at  $z = 6-9$ . The color is scaled by O/C abundance ratio. Gray line shows result of the least-square fitting.

can fall back to the halo due to the deeper gravitational potential well.

We also compare the  $L_{[\text{O III}]} / L_{[\text{C II}]}$  ratio with that of lowSF (green) and noSN (red) cases. In the lowSF case, we set a lower value for the coefficient of Kennicutt–Schmidt relation ( $A$ ) than that of the fiducial case, which induces higher gas density (see also, Y17). The SFR becomes similar in both cases by feedback processes, but the H II volume fraction in the lowSF case is lower, because the dense gas rapidly recombines (see Sec. 4.1). The high density also makes the energy injection by SNe inefficient due to radiative cooling, thus the metal enrichment proceeds faster. These factors lead to very low  $L_{[\text{O III}]} / L_{[\text{C II}]}$  ( $\sim -2.0$  at  $z < 10$ ). On the other hand, the noSN case has similar gas densities as the fiducial case, but SN feedback does not evacuate gas from the halo, resulting in rapid metal enrichment. The O/C abundance ratio stays at low values, resulting in low  $L_{[\text{O III}]} / L_{[\text{C II}]}$  ( $\sim -0.5$ ).

Metallicity in high- $z$  galaxies are observationally estimated using the attenuation by Fe ions in the UV part of the stellar spectrum. However, Cullen et al. (2017) shows that simulated galaxies at  $z \gtrsim 5$  are  $\alpha$ -element enhanced, which is consistent with the observational study of Steidel et al. (2016). They found a factor of  $\sim 5$  difference between stellar and nebular metallicities. Thus the observational metallicity estimate based on Fe abundance does not trace the total metallicity in high- $z$  galaxies. Figure 10 shows that observations of  $L_{[\text{O III}]} / L_{[\text{C II}]}$  ratio could be a useful tool to estimate the total metallicity of galaxies at high- $z$  more precisely. Using a least-square fitting for  $z = 6-9$  galaxies with  $-0.5 < \log(L_{[\text{O III}]} / L_{[\text{C II}]}) < 2.0$ , we derive the following relation for the total metallicity:

$$\log(Z/Z_{\odot}) = -0.37 - 0.52 \log(L_{[\text{O III}]} / L_{[\text{C II}]}) \quad (7)$$

For example, the metallicity of B14-65666 at  $z = 7.15$  (Hashimoto et al. 2019) is estimated to be  $Z = 0.29Z_{\odot}$  using the above relation.

### 3.6 The $(L_{\text{line}}/L_{\text{IR}})$ – $L_{\text{IR}}$ relations

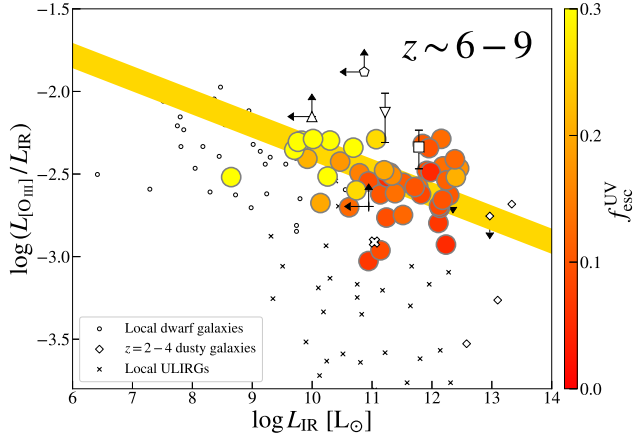
In addition to the ionization of hydrogen and metals, UV radiation from young stars also heats up dust, resulting in IR thermal emission. Therefore, both [O III] and IR luminosities are likely to be related with the SFR. However, depending on the ratio of absorbed energy of ionizing photons between gas and dust, the luminosity ratio changes. Local observations show that  $L_{[\text{O III}]} / L_{\text{IR}}$  and  $L_{[\text{C II}]} / L_{\text{IR}}$  decrease as  $L_{\text{IR}}$  increases (De Looze et al. 2014; Cormier et al. 2015; Díaz-Santos et al. 2014). Cormier et al. (2015) point out that extended dwarf galaxies have higher  $L_{[\text{O III}]} / L_{\text{IR}}$  and suggest the large volume fraction of ionized regions be the reason for this. In addition, recent observations show a similar trend even for high- $z$  galaxies (e.g. Tamura et al. 2019). Here we study the origin of the correlations in  $(L_{\text{line}}/L_{\text{IR}})$ – $L_{\text{IR}}$  relation.

Figure 11 shows the relation between  $L_{[\text{O III}]} / L_{\text{IR}}$  and  $L_{\text{IR}}$  at  $z = 6-9$ . There is a weak negative correlation that is consistent with local star-forming galaxies,  $z \sim 2-4$  dusty star-forming galaxies and ultra-luminous infrared galaxies (ULIRGs). At  $z < 10$ , most of the ionizing photons are absorbed by the gas even in less massive galaxies, resulting in a low escape fraction ( $f_{\text{esc}}^{\text{ion}} \lesssim 0.1$ , see Fig. 4) and a linear  $L_{[\text{O III}]} / \text{SFR}$  relation (equation 5). Meanwhile, UV continuum photons can escape through the direction of low dust column density in the outflowing phase ( $\tau_{\text{UV}} \lesssim 1$ ). We find that the negative correlation is closely related to the escape fraction of UV photons. In A19, we presented the  $L_{\text{IR}}$ –SFR relation at  $z \sim 7$  (Equation 6 in A19):

$$\log(L_{\text{IR}} [L_{\odot}]) = 9.5 + 1.21 \log(\text{SFR} [M_{\odot} \text{ yr}^{-1}]) \quad (8)$$

If the UV light is completely reprocessed into the IR-band, the slope must be unity because UV luminosity is linearly proportional to SFR (e.g., Kennicutt 1998). However, the high UV escape fraction of low-mass galaxies reduces the IR luminosity, resulting in a steeper slope. Combining Eq. (5) and (8), we plot the thick yellow band on the figure. It reproduces our simulation results and observations of high- $z$  galaxies. In addition, our galaxies have high volume fraction of H II regions ( $0.7 < f_{\text{H II}} < 1$ ), which is responsible for higher  $L_{[\text{O III}]} / L_{\text{IR}}$  than in local star-forming galaxies at a specific  $L_{\text{IR}}$ .

Figure 12 shows  $(L_{[\text{C II}]} / L_{\text{IR}})$ – $L_{\text{IR}}$  relation. The model based on the combination of Eq. (6) and (8) is plotted as a thick yellow band. It increases with  $L_{\text{IR}}$  because of the steeper slope of the  $L_{[\text{C II}]} / \text{SFR}$  relation than that of the  $L_{\text{IR}} / \text{SFR}$  relation. Our simulations match the model nicely. However, the luminosity ratios of observed galaxies decreases as  $L_{\text{IR}}$  unlike in our simulations. This discrepancy can be explained by the dust effect. Luhman et al. (2003) suggested the ‘dust-bounded model’, where the dust in H II regions efficiently absorbs UV photons, resulting in inefficient photo-electric heating of polycyclic aromatic hydrocarbons (PAHs) in PDRs. Therefore, the thermally-balanced [C II] cooling also becomes inefficient. Also, if the dust is positively charged, the photo-electric heating and [C II] cooling can be suppressed (Wolfire et al. 1990; Luhman et al. 2003). Combining [C II] 158  $\mu\text{m}$  and CO (3-2) observations at  $z \sim 3$ , Rybak et al. (2019) suggests that high-temperature saturation of  $\text{C}^+$  level populations due to a strong UV radiation field induce the [C II] deficit (Muñoz & Oh 2016). As de-



**Figure 11.** Relation between luminosity ratio  $L_{[\text{OIII}]} / L_{\text{IR}}$  and total IR luminosity  $L_{\text{IR}}$ . Filled circles represent our simulation samples at  $z = 6 - 9$ . The color is scaled by escape fraction of UV photons. Thick yellow line shows combination of our fitting functions (Eq. 5 and 8). Open small circles represent local dwarf galaxies (Madden et al. 2013; Cormier et al. 2015). Open diamonds are for dusty star-forming galaxies at  $z \sim 2 - 4$  (Ferkinhoff et al. 2010; Ivison et al. 2010; Valtchanov et al. 2011; Vishwas et al. 2018). Small crosses are for from local spiral galaxies to ULIRGs (Herrera-Camus et al. 2018a,b). Other open symbols are for  $z \gtrsim 6$  galaxies (Inoue et al. 2016; Carniani et al. 2017; Laporte et al. 2017; Hashimoto et al. 2018; Tamura et al. 2019; Hashimoto et al. 2019).

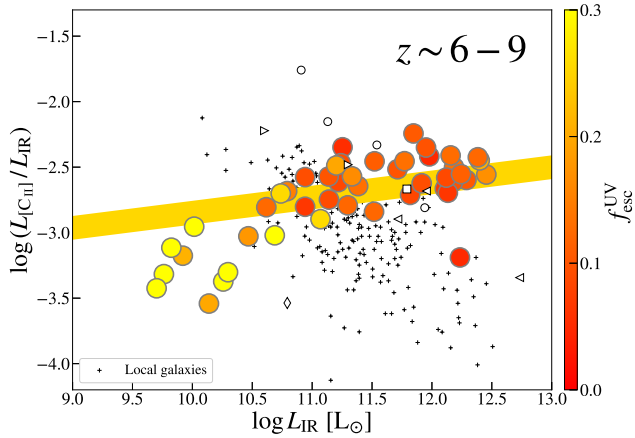


**Figure 12.** Relation between  $L_{[\text{CII}]} / L_{\text{IR}}$  and  $L_{\text{IR}}$ . The meaning of filled circles is the same as in Fig. 11. Thick yellow band shows the combination of Eq. 6 and 8. Small plus symbols represent the local galaxies from LIRGs to ULIRGs (Díaz-Santos et al. 2014). Other open symbols are for  $z \gtrsim 5$  galaxies (Capak et al. 2015; Willott et al. 2015; Knudsen et al. 2017; Decarli et al. 2017; Hashimoto et al. 2019).

scribed in Sec. 2.2, we assume the low dust-to-gas mass ratio in H II cells considering dust destruction in ionized gas. Also, our model does not consider the dust charge. These can be the reasons for differences between our simulations and observations.

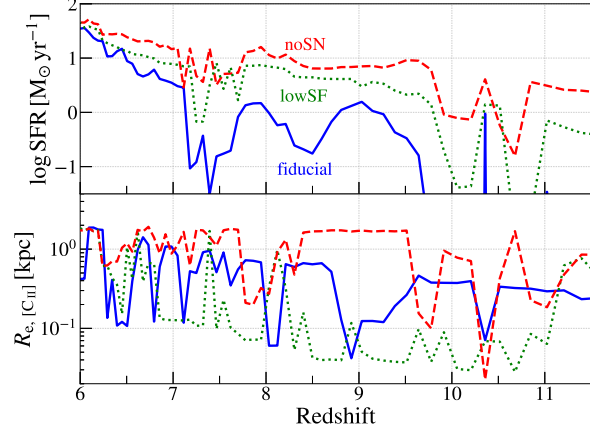


**Figure 13.** Redshift evolution of SFRs (*top panel*) and half-light radii of [C II] intensity maps (*bottom panel*) in the case of Halo-11 (blue solid), Halo-11-noSN (red dashed) and Halo-11-lowSF (green dotted) runs. We set an upper limit of  $R_{e,[\text{CII}]}$  at  $0.1r_{\text{vir}}$  to avoid artificially large sizes due to galaxy mergers.

### 3.7 Galaxy size measured by [C II] line

The size of galaxy was classically considered to be determined by the conservation of angular momentum of accreting gas (Mo et al. 1998). However, recent simulations showed that stellar feedback re-distributes angular momentum and changes galaxy sizes (Genel et al. 2015, Y17). Therefore the galaxy morphology can be used as a test of theoretical feedback models. Recently, Fujimoto et al. (2019) stacked the ALMA data of 18 galaxies at  $z \sim 5 - 7$ , and detected the [C II] emission extended over  $\sim 10$  kpc. The effective radius was larger than the disk scale measured from the rest-UV and FIR continuum emissions.

Our simulated galaxies have disk structures at  $z \lesssim 10$ , and the sizes are affected by SN feedback as described in Y17. In A19, we showed that the UV half-light radius changed within the range of  $\sim 1 - 10\%$  of virial radius ( $r_{\text{vir}}$ ) due to intermittent star formation history. The UV radial profile was dominated by the central star-forming regions in star-burst phases. On the other hand, in outflowing phases, the gas is ejected from the centre and the gravitational potential becomes shallower, resulting in an extended distribution of residual high-mass stars and UV radial profile.

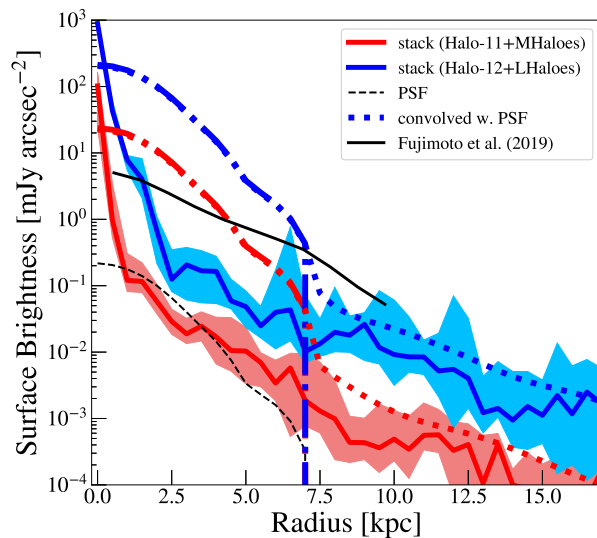
Recent ALMA observations have allowed us to study the kinematics and sizes of distant galaxies via [C II] emission. Thus we here focus on the galaxy size measured by [C II] 158  $\mu\text{m}$  line. Figure 13 shows that the half-light radius of [C II] intensity map changes with intermittent star formation. It is dominated by the emission from central high-density clumps and becomes small ( $\sim 0.1$  kpc) in star-burst phases, while it becomes extended in the outflow phase. In this figure, we set an upper limit to the half-light radius at  $0.1r_{\text{vir}} (\propto M_{\text{h}}^{1/3} (1+z)^{-1})$  to avoid artificially large sizes due to galaxy mergers. At  $z < 8$ , [C II] sizes rapidly changes due to complex clumpy gas structures in the disk. We also find that [C II] size in the lowSF case has lower values than that of the fiducial case, because high-density clumps continuously reside in the central region (see also, Sec. 4.1).

Figure 14 presents the stacked [C II] radial profiles for

$M_h \sim 10^{11} M_\odot$  haloes (red; Halo-11+MHaloes), and for  $M_h \sim 10^{12} M_\odot$  haloes (blue; Halo-12+LHaloes) at  $z \sim 6$ . Here we make the [C II] intensity maps seen from three viewing angles for each halo, and examine the variation. Our simulations show that the surface brightness extension becomes large as the galaxy mass increases. The two solid lines in Fig. 14 show that the intrinsic intensity profiles are very peaky at the inner radii ( $r \lesssim 3$  kpc), and has extended wings in the outskirts which decreases slowly. To mimic the observation by ALMA, we convolve the simulated profiles with the point spread function (PSF) of ALMA in two different ways. The ALMA PSF has a gaussian-like central peak and a long tail with slight negative values (Fujimoto, in private communication). The first method is to fully consider the negative tail of ALMA PSF at  $r > 7$  kpc, which causes abrupt truncation of the convolved profile at  $r \sim 7$  kpc as shown by the dot-dashed lines. The second method is to simply neglect the negative part of PSF and only use the positive gaussian-like peak in the central part for convolution, which results in the dotted curve. In the second method, the central profile is identical with the first method at  $r < 7$  kpc, but the extended outer tail is preserved after the convolution without being subtracted to zero. In both cases, the PSF is normalized to unity, so that the total flux is conserved before and after the convolution. Both cases show that the shape of inner profiles ( $r < 7$  kpc) is completely determined by that of the PSF (because the central intrinsic peak is acting almost like a delta-function), and the contribution from outer radii are negligible. The observational result by Fujimoto et al. (2019) is shown by the black solid line, which extends out to  $r \sim 9.5$  kpc with a shallower slope than the simulation results. They used galaxies with  $-23 \lesssim M_{UV} \lesssim -21$ , which is in the similar range of simulated galaxies in our  $M_h \sim 10^{12} M_\odot$  haloes (see Table 1). Even after the convolution, we find that the simulation results are much steeper than the observed result with higher intensities in the central region. The intensity profile in the outer part ( $r > 7$  kpc) is similar to the observed one by Fujimoto et al. (2019), but is slightly lower at  $r \sim 10$  kpc. These differences in the intensity profiles might give us important clues regarding the physics of feedback in high- $z$  galaxies. In order for our simulations to reproduce the observation, the [C II] flux has to be decreased in the central region by about 1–2 orders of magnitude. As Neri et al. (2014) suggested, the [C II] line of high- $z$  galaxies might be optically thick. The assumption of optically-thin emission in our model would overestimate the central [C II] luminosity. In addition, our simulations do not resolve molecular cloud formation in which  $C^+$  ions will rapidly react to form CO molecules and reduce further central [C II] emission (Narayanan & Krumholz 2017).

Furthermore, a more realistic feedback model might reduce the discrepancy of [C II] luminosity in the outer part. For star-forming galaxies, stellar radiation pressure ejects the gas out of the disk within a few Myr, then the cold gas clouds are further accelerated by the ram pressure of SNe. These processes generate cold outflows with  $\sim 10^4$  K (e.g. Murray et al. 2011; Muratov et al. 2015), and the stacking from various viewing angles might produce the extended [C II] profile.

There are some observational hints from observations on this point already. Using the [C II] stacked data of  $z \sim 5$  galaxies in the ALPINE survey, Ginolfi et al. (2019)



**Figure 14.** Radial profile of [C II] surface brightness. The red solid line and the shade represent median and quartiles for 15 stacked samples ([Halo-11 and MHaloes]  $\times$  3-viewing angles) at  $z \sim 6$ . The blue solid line and the shade are for the stacked data of [Halo-12 and LHaloes]  $\times$  3-viewing angles. The black line represents observational stacking result over 18 galaxies at  $z \sim 6$  (Fujimoto et al. 2019). The simulation profiles are very peaky at the center, and become the dotted and dot-dashed lines after convolving with the point spread function (PSF) for ALMA (see text).

reported a detection of outflows with a velocity of  $\lesssim 500$  km  $s^{-1}$ . They also showed that higher-SFR galaxies have more extended [C II] profiles. We will examine how star formation and feedback models affect [C II] profiles of high- $z$  galaxies in our future work, and will compare with above observations further.

## 4 DISCUSSION

### 4.1 Impact of Star Formation and SN Feedback Models

Physical properties of the first galaxies and their UV/IR continuum fluxes can sensitively depend on the models of star formation and SN feedback (e.g., Wise & Cen 2009; Maio et al. 2011; Johnson et al. 2013; Hopkins et al. 2014; Kimm & Cen 2014; Paardekooper et al. 2015; Yajima et al. 2015, 2017; Behrens et al. 2018; Ma et al. 2019; Arata et al. 2019). In this subsection, we study the impact of star formation and feedback models on metal emission lines.

Figure 15 compares the [O III] and [C II] luminosities from different sub-grid models. In the low-SF run, the central gas density becomes higher than in the fiducial case, which results in inefficient SN feedback due to rapid cooling of injected energy (Yajima et al. 2017). The dense gas also induces rapid hydrogen recombination, resulting in the shrinkage of H II regions. Therefore, the [O III] luminosity becomes smaller by a factor of  $\sim 2$  than in the fiducial case at  $z \sim 6$ . Conversely, [C II] luminosity in the low-SF case is higher than that of fiducial case due to efficient H I cloud formation. Using an analytical model based on the Kennicutt-

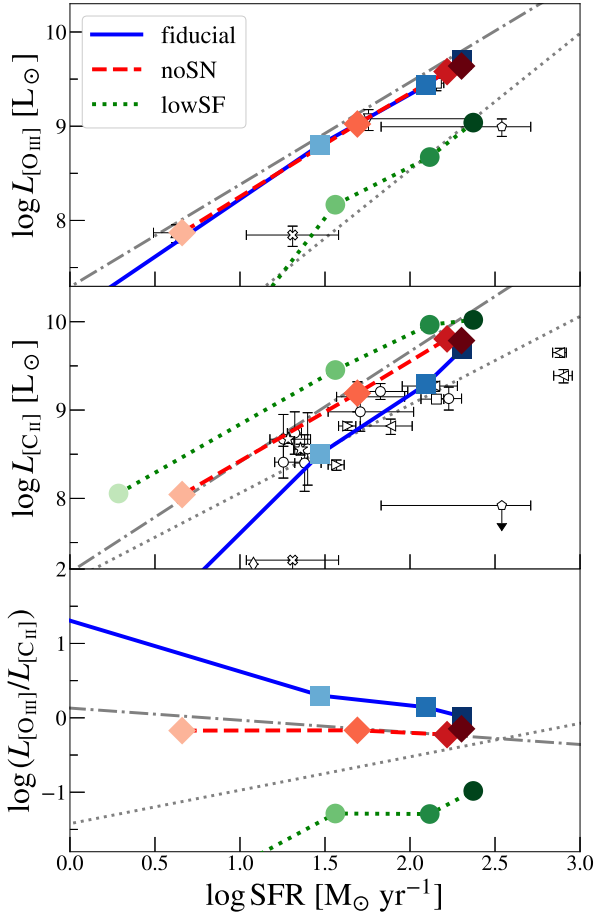


**Figure 15.** Model dependence of relation between SFR and metal line luminosities for Halo-12. The blue solid line and squares represent the fiducial case at  $z = 9, 8, 7$  &  $6$  (lighter to darker). The red dashed line and diamonds are for the no-SN case, and green dotted line and circles are for the low-SF case. The open symbols represent observed galaxies at  $z \sim 6 - 9$  (same as in Fig. 6 and Fig. 7).

Schmidt relation, Ferrara et al. (2019) showed that high- $A$  coefficient could explain the  $[\text{C II}]$  deficiency of high- $z$  galaxies, because it induced low  $\Sigma_g$  at a specific  $\Sigma_{\text{SFR}}$  and the ISM is dominated by hydrogen ionized regions. Our simulation is consistent with their results.

The central density and SFR in the no-SN model are similar to the fiducial run during the star-burst phases (see Fig. 3 in Yajima et al. 2017), resulting in similar volume fraction of  $\text{H II}$  regions, and the  $L_{[\text{O III}]}$ -SFR relations in the two models are very close. On the other hand, the  $[\text{C II}]$  luminosity is higher by a factor of few than that of fiducial case, because carbon enrichment has proceeded earlier (see Fig. 9). We find that our fiducial and noSN models roughly match the observations of local galaxies, while the  $[\text{C II}]$  luminosities of the lowSF model are higher than the observations. Due to these effects the  $L_{[\text{O III}]} / L_{[\text{C II}]}$  changes significantly depending on the star formation and feedback models (bottom panel). Only the fiducial case reproduces the observed negative correlation between the luminosity ratio and SFR.

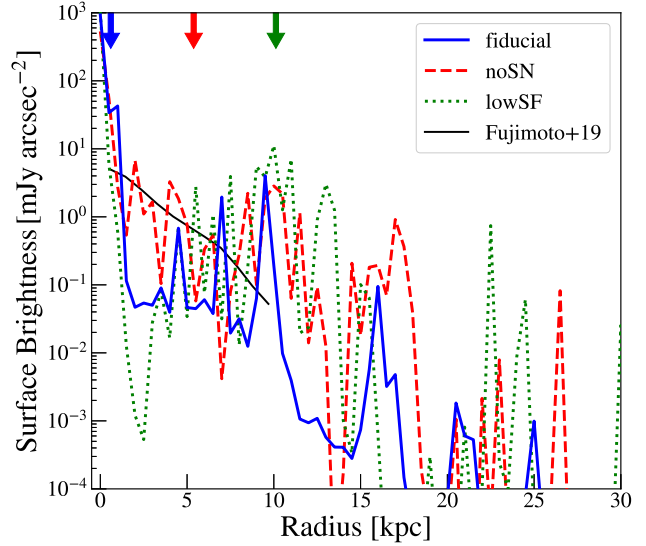


**Figure 16.** Radial profiles of  $[\text{C II}]$  surface brightness of Halo-12 at  $z = 6.45$  in fiducial case (blue solid line), no-SN case (red dashed line) and low-SF case (green dotted line). The arrows represent the half-light radius in each case. In the cases of no-SN and low-SF, many  $[\text{C II}]$ -bright clumps exist in the outer halo, resulting in the extended distribution.

Figure 16 shows the  $[\text{C II}]$  radial profiles for different models at  $z = 6.45$ . In the fiducial case, the SN feedback destroys  $\text{H I}$  clouds in the extended disk, which leads to the concentrated structure. On the other hand, as described above, the other models can have many  $[\text{C II}]$ -bright clumps even at the outer halo. We find that the half-light radius significantly extends in low-SF and no-SN cases. Therefore resolving  $[\text{C II}]$  distribution of individual galaxy would be a key to constrain theoretical models.

## 5 SUMMARY

Combining zoom-in cosmological hydrodynamic simulations and radiative transfer calculations, we have investigated the radiative properties of galaxies at  $z \sim 6 - 15$  focusing on the  $[\text{O III}]$   $88 \mu\text{m}$  and  $[\text{C II}]$   $158 \mu\text{m}$  emission lines. We use 12 haloes whose masses are  $\sim 10^{11} M_{\odot}$  (Halo-11 and MHalo-0, 1, 2, 3) and  $\sim 10^{12} M_{\odot}$  (Halo-12 and LHALo-0, 1, 2, 3, 4, 5) at  $z = 6$ . Our major findings are as follows:

(i) The metal line luminosities rapidly change with intermittent star formation histories due to SN feedback and gas accretion. The  $[\text{O III}]$  line is emitted only during the star-burst phases because  $\text{O}^{2+}$  ions exist in  $\text{H II}$  regions formed by massive stars, while the  $[\text{C II}]$  line is continuously emitted from neutral gas even during the outflowing phases (Fig. 4). We show that, in the case of haloes of  $\sim 10^{11} M_{\odot}$ , the  $[\text{O III}]$  luminosity changes between  $\sim 10^{40} - 10^{42} \text{ erg s}^{-1}$  at  $z < 10$ .

(ii) We find that  $\log L_{[\text{O III}]}$  is linearly proportional to  $\log \text{SFR}$  (Fig. 6). The relation is very close to that of local metal-poor galaxies (De Looze et al. 2014). Meanwhile, the  $\log L_{[\text{C II}]} - \log \text{SFR}$  relation is steeper (slope of  $\sim 1.4$ ) than that of local ones ( $\sim 1 - 1.2$ ) (Fig. 7). We provide fit-



ting formulae for these relations in §3.4. The [O III] surface brightness is  $\gtrsim 1 \text{ mJy arcsec}^{-2}$  with very compact and high-density regions at  $z = 6$ . The comparison of size and surface brightness of [O III] regions with observations can help to constrain physical model of feedback from massive stars.

(iii) In our samples, line luminosity ratio  $L_{[\text{O III}]} / L_{[\text{C II}]}$  decreases from  $\sim 10$  to  $\sim 1$  with increasing bolometric luminosity ( $10^9 L_{\odot} - 10^{12} L_{\odot}$ ) and metallicity ( $0.1 Z_{\odot} - 1 Z_{\odot}$ ), which is in good agreement with local and high- $z$  observations (Fig. 8). We find that  $\log(\text{O/C})$  abundance ratio is initially dominated by the oxygen enrichment of Type-II SNe, and decreases from  $\sim 0.9$  to  $\sim 0.5$  due to carbon-rich wind from AGB stars. Thus, the  $L_{[\text{O III}]} / L_{[\text{C II}]}$  ratio decreases with galaxy evolution and metal enrichment. We provide fitting formula for the relation between  $L_{[\text{O III}]} / L_{[\text{C II}]}$  and metallicity, which could be used to constrain the metallicity of high- $z$  galaxies in the future from the line ratio.

(iv) The luminosity ratio  $\log(L_{[\text{O III}]} / L_{\text{IR}})$  of our samples weakly correlates with  $\log L_{\text{IR}}$  with the slope of  $\sim -0.14$ , and the negative trend is consistent with high- $z$  observations. We find that the relation depends on the escape fraction of UV photons. In the case of low-mass galaxies, most of UV photons can escape without dust absorption. Therefore, the conversion fraction from UV to IR radiation via dust absorption increases with the galaxy mass. This results in making the  $\log L_{\text{IR}} - \log \text{SFR}$  relation steeper (slope of  $\sim 1.2$ ). On the other hand, we see a positive correlation in the  $\log(L_{[\text{C II}]} / L_{\text{IR}}) - \log L_{\text{IR}}$  relation, which is inconsistent with observations (Fig. 12). We argue that this inconsistency might be alleviated using a more detailed dust model.

(v) To clarify the impact of sub-grid models of star formation and SN feedback on our results, we examine simulations with lower star formation efficiency (lowSF) and without supernova feedback (noSN). We find that, in the lowSF case, H II regions are not as much extended due to high-density gas and rapid recombination, which results in lower  $L_{[\text{O III}]}$  and higher  $L_{[\text{C II}]}$  than in the fiducial case by order unity. In the noSN case, the density structure is similar to that of the fiducial case, resulting in similar [O III] luminosities. However, the galaxies in the noSN model experience rapid metal enrichment by Type-II SNe and AGB stars and have high carbon abundances. Therefore the [C II] luminosity is higher than in the fiducial run. We find that only the fiducial runs reproduce the observed negative correlation between  $L_{[\text{O III}]} / L_{[\text{C II}]}$  and  $L_{\text{bol}}$ .

## ACKNOWLEDGMENTS

We are grateful to Dr. Inoue for helpful comments on model calculations, and to Dr. Fujimoto for useful discussions on ALMA PSF. Numerical computations were carried out on the Cray XC30 & XC50 at the Center for Computational Astrophysics, National Astronomical Observatory of Japan, and the OCTOPUS at the Cybermedia Center, Osaka University as part of the HPCI system Research Project (hp180063, hp190050). This work is supported in part by the MEXT/JSPS KAKENHI Grant Number JP17H04827 (H.Y.), 18H04570 (H.Y.) and JP17H01111 (K.N.). KN acknowledges the travel support from the Kavli IPMU, World

Premier Research Center Initiative (WPI), where part of this work was conducted.

## REFERENCES

- Aggarwal K. M., Keenan F. P., 1999, *ApJS*, 123, 311  
 Altay G., Theuns T., Schaye J., Crighton N. H. M., Dalla Vecchia C., 2011, *ApJ*, 737, L37  
 Arata S., Yajima H., Nagamine K., 2018, *MNRAS*, 475, 4252  
 Arata S., Yajima H., Nagamine K., Li Y., Khochfar S., 2019, *MNRAS*, 488, 2629  
 Behrens C., Pallottini A., Ferrara A., Gallerani S., Vallini L., 2018, *MNRAS*, 477, 552  
 Berg D. A., Erb D. K., Henry R. B. C., Skillman E. D., McQuinn K. B. W., 2019, arXiv e-prints  
 Bird S., Vogelsberger M., Sijacki D., Zaldarriaga M., Springel V., Hernquist L., 2013, *MNRAS*, 429, 3341  
 Bowler R. A. A., Bourne N., Dunlop J. S., McLure R. M., McLeod D. J., 2018, ArXiv e-prints  
 Brocklehurst M., 1971, *MNRAS*, 153, 471  
 Burke J. R., Silk J., 1974, *ApJ*, 190, 1  
 Capak P. L., Carilli C., Jones G., Casey C. M., Riechers D., Sheth K., Carollo C. M., Ilbert O., Karim A., Lefevre O., Lilly S., Scoville N., Smolcic V., Yan L., 2015, *Nature*, 522, 455  
 Carniani S., Maiolino R., Pallottini A., Vallini L., Pentericci L., Ferrara A., Castellano M., Vanzella E., Grazian A., Gallerani S., Santini P., Wagg J., Fontana A., 2017, *A&A*, 605, A42  
 Chabrier G., 2003, *PASP*, 115, 763  
 Cormier D., Lebouteiller V., Madden S. C., Abel N., Hony S., Galliano F., Baes M., Barlow M. J. e. a., 2012, *A&A*, 548, A20  
 Cormier D., Madden S. C., Lebouteiller V., Abel N., Hony S., Galliano F., Rémy-Ruyer A., Bigiel F. e. a., 2015, *A&A*, 578, A53  
 Croxall K. V., Smith J. D., Pellegrini E., Groves B., Bolatto A., Herrera-Camus R., Sandstrom K. M., Draine B., Wolfire M. G., Armus L., Boquien M., Brandl B., Dale D., Galametz M., Hunt L., Kennicutt R. J., Kreckel K., Rigopoulou D., van der Werf P., Wilson C., 2017, *The Astrophysical Journal*, 845, 96  
 Cullen F., McLure R. J., Khochfar S., Dunlop J. S., Dalla Vecchia C., 2017, *MNRAS*, 470, 3006  
 da Cunha E., Groves B., Walter F., Decarli R., Weiss A., Bertoldi F., Carilli C., Daddi E., Elbaz D., Ivison R., Maiolino R., Riechers D., Rix H.-W., Sargent M., Smail I., 2013, *ApJ*, 766, 13  
 Dalla Vecchia C., Schaye J., 2012, *MNRAS*, 426, 140  
 Davis A. J., Khochfar S., Dalla Vecchia C., 2014, *MNRAS*, 443, 985  
 De Looze I., Cormier D., Lebouteiller V., Madden S., Baes M., Bendo G. J., Boquien M., et al. B., 2014, *A&A*, 568, A62  
 Decarli R., Walter F., Venemans B. P., Bañados E., Bertoldi F., Carilli C., Fan X., Farina E. P., Mazzucchelli C., Riechers D., Rix H. W., Strauss M. A., Wang R., Yang Y., 2017, *Nature*, 545, 457  
 Dekel A., Birnboim Y., 2006, *MNRAS*, 368, 2

- Díaz-Santos T., Armus L., Charmandaris V., Stacey G., Murphy E. J., Haan S., Stierwalt S., Malhotra S. e. a., 2014, *The Astrophysical Journal*, 788, L17
- Draine B. T., Dale D. A., Bendo G., Gordon K. D., Smith J. D. T., Armus L., Engelbracht C. W., Helou G., Kennicutt Jr. R. C., Li A., Roussel H., Walter F., Calzetti D., Moustakas J., Murphy E. J., Rieke G. H., Bot C., Hollenbach D. J., Sheth K., Teplitz H. I., 2007, *ApJ*, 663, 866
- Ferkinhoff C., Hailey-Dunsheath S., Nikola T., Parshley S. C., Stacey G. J., Benford D. J., Staguhn J. G., 2010, *ApJ*, 714, L147
- Ferland G. J., Korista K. T., Verner D. A., Ferguson J. W., Kingdon J. B., Verner E. M., 1998, *PASP*, 110, 761
- Ferrara A., Vallini L., Pallottini A., Gallerani S., Carniani S., Kohandel M., Decataldo D., Behrens C., 2019, *MNRAS*, 489, 1
- Fujimoto S., Ouchi M., Ferrara A., Pallottini A., Ivison R. J., Behrens C., Gallerani S., Arata S. e. a., 2019, *arXiv e-prints*, arXiv:1902.06760
- Genel S., Fall S. M., Hernquist L., Vogelsberger M., Snyder G. F., Rodriguez-Gomez V., Sijacki D., Springel V., 2015, *ApJ*, 804, L40
- Genzel R., Tacconi L. J., Gracia-Carpio J., Sternberg A., Cooper M. C., Shapiro K., Bolatto A., Bouché N. et al., 2010, *MNRAS*, 407, 2091
- Ginolfi M., Jones G. C., Bethermin M., Fudamoto Y., Loiacono F., Fujimoto S., Fevre L., Faisst A., Schaerer D., Cassata P., Silverman J. D., Yan L., Capak P., Bardelli S., Boquien M., Carraro R., Dessauges-Zavadsky M., Gialisco M., Gruppioni C., Ibar E., Khusanova Y., Lemaux B. C., Maiolino R., Narayanan D., Oesch P., Pozzi F., Rodighiero G., Talia M., Toft S., Vallini L., Vergani D., Zamorani G., 2019, *arXiv e-prints*, arXiv:1910.04770
- Glover S. C. O., Jappsen A. K., 2007, *ApJ*, 666, 1
- Goldsmith P. F., Langer W. D., Pineda J. L., Velusamy T., 2012, *ApJS*, 203, 13
- Haardt F., Madau P., 2012, *ApJ*, 746, 125
- Hahn O., Abel T., 2011, *MNRAS*, 415, 2101
- Harikane Y., Ouchi M., Inoue A. K., Matsuoka Y., Tamura Y., Bakx T., Fujimoto S., Moriwaki K., Ono Y., Nagao T., Tadaki K.-i., Kojima T., Shibuya T., Egami E., Ferrara A., Gallerani S., Hashimoto T., Kohno K., Matsuda Y., Matsuo H., Pallottini A., Sugahara Y., Vallini L., 2019, *arXiv e-prints*, arXiv:1910.10927
- Hashimoto T., Inoue A. K., Mawatari K., Tamura Y., Matsuo H., Furusawa H., Harikane Y., Shibuya T., Knudsen K. K., Kohno K., Ono Y., Zackrisson E., Okamoto T., Kashikawa N., Oesch P. A., Ouchi M., Ota K., Shimizu I., Taniguchi Y., Umehata H., Watson D., 2019, *PASJ*, 71, 71
- Hashimoto T., Laporte N., Mawatari K., Ellis R. S., Inoue A. K., Zackrisson E., Roberts-Borsani G., Zheng W. et al., 2018, *Nature*, 557, 392
- Herrera-Camus R., Sturm E., Graciá-Carpio J., Lutz D., Contursi A., Veilleux S., Fischer J., González-Alfonso E. e. a., 2018a, *The Astrophysical Journal*, 861, 94
- , 2018b, *The Astrophysical Journal*, 861, 95
- Hopkins P. F., Kereš D., Oñorbe J., Faucher-Giguère C.-A., Quataert E., Murray N., Bullock J. S., 2014, *MNRAS*, 445, 581
- Inoue A. K., 2011, *MNRAS*, 415, 2920
- Inoue A. K., Shimizu I., Tamura Y., Matsuo H., Okamoto T., Yoshida N., 2014, *ApJ*, 780, L18
- Inoue A. K., Tamura Y., Matsuo H., Mawatari K., Shimizu I., Shibuya T., Ota K., Yoshida N. et al., 2016, *Science*, 352, 1559
- Ivison R. J., Swinbank A. M., Swinyard B., Smail I., Pearson C. P., Rigopoulou D., Polehampton E., Baluteau J. P. e. a., 2010, *A&A*, 518, L35
- Johnson J. L., Dalla Vecchia C., Khochfar S., 2013, *MNRAS*, 428, 1857
- Katz H., Galligan T. P., Kimm T., Rosdahl J., Haehnelt M. G., Blaizot J., Devriendt J., Slyz A., Laporte N., Ellis R., 2019, *MNRAS*, 487, 5902
- Kennicutt Jr. R. C., 1998, *ARA&A*, 36, 189
- Kimm T., Cen R., 2014, *ApJ*, 788, 121
- Knudsen K. K., Watson D., Frayer D., Christensen L., Gallazzi A., Michałowski M. J., Richard J., Zavala J., 2017, *MNRAS*, 466, 138
- Lagache G., Cousin M., Chatzikos M., 2018, *A&A*, 609, A130
- Laporte N., Ellis R. S., Boone F., Bauer F. E., Quénard D., Roberts-Borsani G. W., Pelló R., Pérez-Fournon I., Streblyanska A., 2017, *ApJ*, 837, L21
- Laporte N., Katz H., Ellis R. S., Lagache G., Bauer F. E., Boone F., Inoue A. K., Hashimoto T. e. a., 2019, *MNRAS*, 487, L81
- Leitherer C., Schaerer D., Goldader J. D., Delgado R. M. G., Robert C., Kune D. F., de Mello D. F., Devost D., Heckman T. M., 1999, *ApJS*, 123, 3
- Li Y., Hopkins P. F., Hernquist L., Finkbeiner D. P., Cox T. J., Springel V., Jiang L., Fan X., Yoshida N., 2008, *ApJ*, 678, 41
- Luhman M. L., Satyapal S., Fischer J., Wolfire M. G., Sturm E., Dudley C. C., Lutz D., Genzel R., 2003, *ApJ*, 594, 758
- Ma X., Hayward C. C., Casey C. M., Hopkins P. F., Quataert E., Liang L., Faucher-Giguère C.-A., Feldmann R., Kereš D., 2019, *arXiv e-prints*
- Madden S. C., Rémy-Ruyer A., Galametz M., Cormier D., Lebouteiller V., Galliano F., Hony S., Bendo G. J. e. a., 2013, *PASP*, 125, 600
- Maio U., Khochfar S., Johnson J. L., Ciardi B., 2011, *MNRAS*, 414, 1145
- Marigo P., 2001, *A&A*, 370, 194
- Marrone D. P., Spilker J. S., Hayward C. C., Vieira J. D., Aravena M., Ashby M. L. N., Bayliss M. B., Béthermin M. et al., 2018, *Nature*, 553, 51
- Mo H. J., Mao S., White S. D. M., 1998, *MNRAS*, 295, 319
- Moriwaki K., Yoshida N., Shimizu I., Harikane Y., Matsuda Y., Matsuo H., Hashimoto T., Inoue A. K., Tamura Y., Nagao T., 2018, *MNRAS*, 481, L84
- Muñoz J. A., Oh S. P., 2016, *MNRAS*, 463, 2085
- Muratov A. L., Kereš D., Faucher-Giguère C.-A., Hopkins P. F., Quataert E., Murray N., 2015, *MNRAS*, 454, 2691
- Murray N., Ménard B., Thompson T. A., 2011, *ApJ*, 735, 66
- Nagamine K., Choi J.-H., Yajima H., 2010, *ApJ*, 725, L219
- Nagamine K., Wolfe A. M., Hernquist L., 2006, *ApJ*, 647, 60
- Nahar S. N., 1999, *ApJS*, 120, 131
- Nahar S. N., Pradhan A. K., 1997, *ApJS*, 111, 339
- Narayanan D., Krumholz M. R., 2017, *MNRAS*, 467, 50

- Neri R., Downes D., Cox P., Walter F., 2014, *A&A*, 562, A35
- Nussbaumer H., Storey P. J., 1981, *A&A*, 99, 177
- Olsen K., Greve T. R., Narayanan D., Thompson R., Davé R., Niebla Rios L., Stawinski S., 2017, *ApJ*, 846, 105
- Paardekooper J.-P., Khochfar S., Dalla Vecchia C., 2015, *MNRAS*, 451, 2544
- Pallottini A., Ferrara A., Bovino S., Vallini L., Gallerani S., Maiolino R., Salvadori S., 2017a, *MNRAS*, 471, 4128
- Pallottini A., Ferrara A., Decataldo D., Gallerani S., Vallini L., Carniani S., Behrens C., Kohandel M., Salvadori S., 2019, *MNRAS*, 487, 1689
- Pallottini A., Ferrara A., Gallerani S., Vallini L., Maiolino R., Salvadori S., 2017b, *MNRAS*, 465, 2540
- Portinari L., Chiosi C., Bressan A., 1998, *A&A*, 334, 505
- Rahmati A., Pawlik A. H., Raičević M., Schaye J., 2013, *MNRAS*, 430, 2427
- Reynolds C. S., Ward M. J., Fabian A. C., Celotti A., 1997, *MNRAS*, 291, 403
- Richings A. J., Schaye J., Oppenheimer B. D., 2014, *MNRAS*, 440, 3349
- Rybak M., Calistro Rivera G., Hodge J. A., Smail I., Walter F., van der Werf P., da Cunha E., Chen C.-C. e. a., 2019, *The Astrophysical Journal*, 876, 112
- Saitoh T. R., 2017, *AJ*, 153, 85
- Schaye J., Dalla Vecchia C., 2008, *MNRAS*, 383, 1210
- Schaye J., Dalla Vecchia C., Booth C. M., Wiersma R. P. C., Theuns T., Haas M. R., Bertone S., Duffy A. R., McCarthy I. G., van de Voort F., 2010, *MNRAS*, 402, 1536
- Seon K.-I., Edelstein J., Korpela E., Witt A., Min K.-W., Han W., Shinn J., Kim I.-J. e. a., 2011, *ApJS*, 196, 15
- Smit R., Bouwens R. J., Carniani S., Oesch P. A., Labbé I., Illingworth G. D., van der Werf P., Bradley L. D., Gonzalez V., Hodge J. A., Holwerda B. W., Maiolino R., Zheng W., 2018, *Nature*, 553, 178
- Springel V., 2005, *MNRAS*, 364, 1105
- Steidel C. C., Strom A. L., Pettini M., Rudie G. C., Reddy N. A., Trainor R. F., 2016, *ApJ*, 826, 159
- Tacconi L. J., Neri R., Genzel R., Combes F., Bolatto A., Cooper M. C., Wuyts S., Bournaud F. et al., 2013, *ApJ*, 768, 74
- Tamura Y., Mawatari K., Hashimoto T., Inoue A. K., Zackrisson E., Christensen L., Binggeli C., Matsuda Y. e. a., 2019, *ApJ*, 874, 27
- Vallini L., Gallerani S., Ferrara A., Pallottini A., Yue B., 2015, *ApJ*, 813, 36
- Valtchanov I., Virdee J., Ivison R. J., Swinyard B., van der Werf P., Rigopoulou D., da Cunha E., Lupu R. e. a., 2011, *MNRAS*, 415, 3473
- Verner D. A., Ferland G. J., Korista K. T., Yakovlev D. G., 1996, *ApJ*, 465, 487
- Vishwas A., Ferkinhoff C., Nikola T., Parshley S. C., Schoenwald J. P., Stacey G. J., Higdon S. J. U., Higdon J. L., Weiss A., Güsten R., Menten K. M., 2018, *ApJ*, 856, 174
- Watson D., Christensen L., Knudsen K. K., Richard J., Gallazzi A., Michałowski M. J., 2015, *Nature*, 519, 327
- Webber W. R., 1998, *The Astrophysical Journal*, 506, 329
- Wiersma R. P. C., Schaye J., Smith B. D., 2009a, *MNRAS*, 393, 99
- Wiersma R. P. C., Schaye J., Theuns T., Dalla Vecchia C., Tornatore L., 2009b, *MNRAS*, 399, 574
- Willott C. J., Carilli C. L., Wagg J., Wang R., 2015, *ApJ*, 807, 180
- Wise J. H., Cen R., 2009, *ApJ*, 693, 984
- Wolfire M. G., McKee C. F., Hollenbach D., Tielens A. G. G. M., 2003, *ApJ*, 587, 278
- Wolfire M. G., Tielens A. G. G. M., Hollenbach D., 1990, *ApJ*, 358, 116
- Yajima H., Choi J.-H., Nagamine K., 2011, *MNRAS*, 412, 411
- , 2012a, *MNRAS*, 427, 2889
- Yajima H., Li Y., Zhu Q., Abel T., 2012b, *Monthly Notices of the Royal Astronomical Society*, 424, 884
- , 2015, *ApJ*, 801, 52
- Yajima H., Li Y., Zhu Q., Abel T., Gronwall C., Ciardullo R., 2014, *MNRAS*, 440, 776
- Yajima H., Nagamine K., Zhu Q., Khochfar S., Dalla Vecchia C., 2017, *ApJ*, 846, 30

## APPENDIX A: COMPARISON WITH CLOUDY

We compare [O III]  $88\mu\text{m}$  luminosity in our model with that of CLOUDY model (e.g. Ferland et al. 1998; Inoue 2011; Inoue et al. 2014). The CLOUDY table gives us luminosity ratio of [O III]  $88\mu\text{m}$  to H $\beta$  lines as a function of density ( $n$ ), ionization parameter ( $U \equiv \Phi/n_e c$ , where  $\Phi$  is flux of hydrogen ionizing photons), and metallicity ( $Z$ ), which is based on radiative transfer calculations assuming plane-parallel geometry and pressure equilibrium. The range of parameter are  $Z/Z_\odot = 5 \times 10^{-3} - 2.5$ ,  $U = 10^{-4} - 10^{-1}$  and  $n = 10 - 10^3 \text{ cm}^{-3}$ . The input stellar spectrum is produced by the STARBURST99 with Salpeter IMF [0.1–100  $M_\odot$ ], constant star formation for 10 Myr, and the same stellar metallicity with gaseous component (Inoue et al. 2014). We use the values of  $n, U, Z$  in each cell, which are the result of ionization RT calculation by ART<sup>2</sup> code, and refer to the CLOUDY table for [O III] emissivity ( $\epsilon_{\text{cl}} \equiv L_{[\text{O III}]}^{\text{cl}}/L_{\text{H}\beta}^{\text{cl}}$ ).

To obtain [O III] emissivity in our model ( $\epsilon$ ), we divide  $L_{[\text{O III}]}$  by H $\beta$  luminosity,  $L_{\text{H}\beta} = \alpha_{\text{H}\beta}^{\text{eff}}(T)n_p n_e h\nu_{\text{H}\beta} V_{\text{cell}}$ , where  $\alpha_{\text{H}\beta}^{\text{eff}}(T)$  is the effective recombination coefficient (Brocklehurst 1971) and  $n_p$  ( $n_e$ ) is the proton (electron) density in the cell.

Figure A1 shows the ratio of  $\epsilon$  to  $\epsilon_{\text{cl}}$  as a function of metallicity. For most of the cells,  $\epsilon/\epsilon_{\text{cl}}$  is almost unity, which implies that our simple emission model is in good agreement with CLOUDY. Total [O III] luminosity is dominated by the contribution from cells with  $|\log \epsilon/\epsilon_{\text{cl}}| < 0.5$  ( $\sim 72\%$ ). Here we focus on the origin of the differences between our model calculation and CLOUDY. There are two-types of outliers at  $\log(\epsilon/\epsilon_{\text{cl}}) > 0.5$ : low- $U$  cells ( $\log U \sim -4$ ) and high-density cells ( $n \gtrsim 500 \text{ cm}^{-3}$ ). In the former case, CLOUDY predicts that weak radiation field ionizes the surface of plane-parallel gas ( $N \lesssim 10^{19} \text{ cm}^{-2}$ ), and [O III] is emitted only from the thin layer. Meanwhile, if the electron fraction of a cell is higher than 0.5, our model calculates optically-thin oxygen ionization equilibrium in the whole cell volume and obtains O<sup>2+</sup> abundance, which would overestimate [O III] emissivity. In the later case (indicated by yellow points in Fig. A1), the emissivity in CLOUDY rapidly decreases with increasing density, because the density exceeds the critical den-

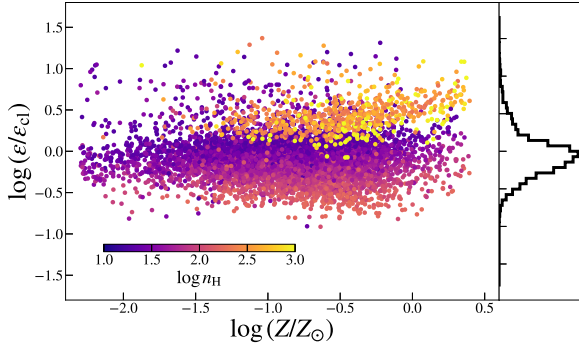


**Figure A1.** Comparison of [O III] emissivity in our model and CLOUDY. Left panel shows the distribution of emissivity ratio  $\epsilon/\epsilon_{\text{cl}}$ , where  $\epsilon$  and  $\epsilon_{\text{cl}}$  is the luminosity ratio of [O III]  $88\ \mu\text{m}$  and H $\beta$  lines computed by each model, in Halo-11 at  $z = 6.0$  as a function of metallicity. The color is scaled by gas density. Right panel shows probability distribution function of  $\log(\epsilon/\epsilon_{\text{cl}})$ .

sity for transition of  $^3\text{P}_1 \rightarrow ^3\text{P}_0$ . Meanwhile, our model predicts that the critical density is higher by a factor of  $\sim 3$  ( $1.74 \times 10^3\ \text{cm}^{-3}$  at  $T = 10^4\ \text{K}$ ), thus the emissivity increases with density. The difference probably comes from referred collision strength  $\Omega$  (Aggarwal & Keenan 1999).

As described above, CLOUDY uses input spectrum assuming a simple stellar population. However, the actual SED would be the sum of various stellar populations with different ages and metallicities, which could be more complex. Also, CLOUDY assumes a solar abundance ratio, but the chemical abundance in high- $z$  galaxies might be very different from our Galaxy. Our model calculates  $\text{O}^{2+}$  abundance under the complex SEDs, and the oxygen enrichment by SNe and AGB stars is tracked by particles separately. Thus, we argue that, at least for the SED treatment, our model is doing a more appropriate treatment for estimating [O III] emission in high- $z$  galaxies.

## APPENDIX B: THE CMB EFFECT

Here we estimate the CMB effect onto [C II]  $158\ \mu\text{m}$  luminosity (e.g. Goldsmith et al. 2012). The population of two energy levels is determined by the rate equation:

$$n_{\text{u}}(A_{\text{ul}} + B_{\text{ul}}J_{\nu} + C_{\text{ul}}) = n_{\text{l}}(B_{\text{lu}}J_{\nu} + C_{\text{lu}}), \quad (\text{B1})$$

where  $n_{\text{u}}(n_{\text{l}})$  is number density of  $\text{C}^+$  ions in the upper (lower) level, and  $J_{\nu}$  is the mean intensity of background radiation at  $158\ \mu\text{m}$ . We assume an escape probability of  $\beta = 1$ , and a black-body spectra  $J_{\nu} = B_{\nu}(T_{\text{CMB}})$ . The  $C_{\text{lu}}$  term is sum of collision rate with electrons ( $e^-$ ), hydrogen atoms ( $\text{H}^0$ ) and hydrogen molecules ( $\text{H}_2$ ) (Glover & Jappsen 2007). The  $C_{\text{lu}}$  and  $C_{\text{ul}}$  are related to each other by detailed balance. The emergent luminosity is calculated by Equation (4). In diffuse ISM, the stimulated absorption rate ( $n_{\text{l}}B_{\text{lu}}J_{\nu}$ ) is higher than stimulated emission rate ( $n_{\text{u}}B_{\text{ul}}J_{\nu}$ ), thus the CMB increases  $n_{\text{u}}/n_{\text{l}}$  ratio and reduces [C II] luminosity.

Figure B1 shows how much [C II] emission is attenuated by CMB at  $z = 7.0$ . For a low temperature gas ( $T \lesssim 100\ \text{K}$ ), the CMB effect becomes significant compared to collisional excitation, resulting in a reduction of luminosity  $\gtrsim 3\%$  (see

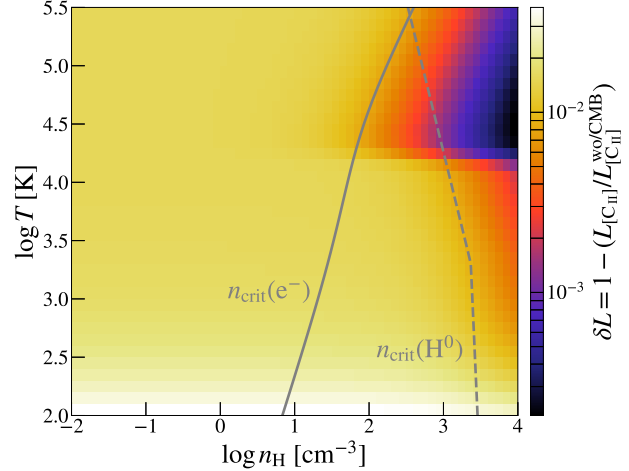


**Figure B1.** The CMB effect to [C II]  $158\ \mu\text{m}$  luminosity at  $z = 7.0$  as a function of hydrogen nuclei density and temperature. Color-scale indicates the reduction strength,  $\delta L = 1 - (L_{[\text{C II}]} / L_{[\text{C II}]^{\text{wo/CMB}}})$ , where  $L_{[\text{C II}]}$  ( $L_{[\text{C II}]^{\text{wo/CMB}}}$ ) is the emergent [C II] luminosity with (without) the CMB stimulated emission and absorption. Gray solid line and dashed line represent the critical densities of electrons ( $n_{\text{crit}}(e^-)$ ) and hydrogen atoms ( $n_{\text{crit}}(\text{H}^0)$ ), respectively.

also, Lagache et al. 2018). At  $T \sim 10^4\ \text{K}$ , the densities of  $e^-$  and  $\text{H}^0$  dramatically change due to hydrogen recombination, thus the collision partner for  $\text{C}^+$  ions switches. If gas density is higher than the critical density of the collision partner, the rate equation is dominated by the collision terms, and as a result, the CMB effect becomes negligible. Note that gas temperature in our simulations is higher than  $10^3\ \text{K}$  (Fig. 3), thus the CMB affects [C II] luminosity only by a few percent.